

# SANDIA REPORT

SAND2013-8111

Unlimited Release

Printed September 2013

## An Interface Tracking Model for Droplet Electrocoalescence

Lindsay Crowl Erickson

Prepared by  
Sandia National Laboratories  
Albuquerque, New Mexico 87185 and Livermore, California 94550

Sandia National Laboratories is a multi-program laboratory managed and operated by Sandia Corporation, a wholly owned subsidiary of Lockheed Martin Corporation, for the U.S. Department of Energy's National Nuclear Security Administration under contract DE-AC04-94AL85000.

Approved for public release; further dissemination unlimited.



**Sandia National Laboratories**

Issued by Sandia National Laboratories, operated for the United States Department of Energy by Sandia Corporation.

**NOTICE:** This report was prepared as an account of work sponsored by an agency of the United States Government. Neither the United States Government, nor any agency thereof, nor any of their employees, nor any of their contractors, subcontractors, or their employees, make any warranty, express or implied, or assume any legal liability or responsibility for the accuracy, completeness, or usefulness of any information, apparatus, product, or process disclosed, or represent that its use would not infringe privately owned rights. Reference herein to any specific commercial product, process, or service by trade name, trademark, manufacturer, or otherwise, does not necessarily constitute or imply its endorsement, recommendation, or favoring by the United States Government, any agency thereof, or any of their contractors or subcontractors. The views and opinions expressed herein do not necessarily state or reflect those of the United States Government, any agency thereof, or any of their contractors.

Printed in the United States of America. This report has been reproduced directly from the best available copy.

Available to DOE and DOE contractors from  
U.S. Department of Energy  
Office of Scientific and Technical Information  
P.O. Box 62  
Oak Ridge, TN 37831

Telephone: (865) 576-8401  
Facsimile: (865) 576-5728  
E-Mail: [reports@adonis.osti.gov](mailto:reports@adonis.osti.gov)  
Online ordering: <http://www.osti.gov/bridge>

Available to the public from  
U.S. Department of Commerce  
National Technical Information Service  
5285 Port Royal Rd  
Springfield, VA 22161

Telephone: (800) 553-6847  
Facsimile: (703) 605-6900  
E-Mail: [orders@ntis.fedworld.gov](mailto:orders@ntis.fedworld.gov)  
Online ordering: <http://www.ntis.gov/help/ordermethods.asp?loc=7-4-0#online>



# An Interface Tracking Model for Droplet Electrocoalescence

Lindsay Crowl Erickson

## Abstract

This report describes an Early Career Laboratory Directed Research and Development (LDRD) project to develop an interface tracking model for droplet electrocoalescence. Many fluid-based technologies rely on electrical fields to control the motion of droplets, e.g. microfluidic devices for high-speed droplet sorting, solution separation for chemical detectors, and purification of biodiesel fuel. Precise control over droplets is crucial to these applications. However, electric fields can induce complex and unpredictable fluid dynamics. Recent experiments (Ristenpart *et al.* 2009) have demonstrated that oppositely charged droplets bounce rather than coalesce in the presence of strong electric fields. A transient aqueous bridge forms between approaching drops prior to pinch-off. This observation applies to many types of fluids, but neither theory nor experiments have been able to offer a satisfactory explanation. Analytic hydrodynamic approximations for interfaces become invalid near coalescence, and therefore detailed numerical simulations are necessary. This is a computationally challenging problem that involves tracking a moving interface and solving complex multi-physics and multi-scale dynamics, which are beyond the capabilities of most state-of-the-art simulations. An interface-tracking model for electro-coalescence can provide a new perspective to a variety of applications in which interfacial physics are coupled with electrodynamics, including electro-osmosis, fabrication of microelectronics, fuel atomization, oil dehydration, nuclear waste reprocessing and solution separation for chemical detectors. We present a conformal decomposition finite element (CDFEM) interface-tracking method for the electrohydrodynamics of two-phase flow to demonstrate electro-coalescence. CDFEM is a sharp interface method that decomposes elements along fluid-fluid boundaries and uses a level set function to represent the interface.

# Acknowledgments

First and foremost the author would like to gratefully acknowledge David Noble for his fundamental involvement in the CDFEM implementation of this model and his mentorship support and guidance during the course of this project. The author is thankful to the SIERRA thermal fluids team - specifically Sam Subia and Scott Roberts - for their involvement in the code development effort, William Ristenpart (UC Davis) for experimental inspiration, Greg Wagner and Jeremy Templeton for program development and support, and David Martin (graduate student intern, UC Merced) for his verification work and unit analysis. This work was funded under LDRD Project Number 155327 and Title “Interface-Tracking Hydrodynamic Model for Droplet Electrocoalescence.”

# Contents

<b>1</b>	<b>Introduction</b>	<b>9</b>
1.1	Applications and inspiration	9
1.2	Overview of numerical approaches	12
<b>2</b>	<b>Governing Equations</b>	<b>15</b>
2.1	Fluid equations	15
2.1.1	Navier-Stokes equations	15
2.1.2	Electric force in the momentum equation	15
2.1.3	Magnetic versus electric time scales	16
2.2	The voltage equation	17
2.3	Charge distribution	17
2.3.1	Charged species	17
2.3.2	Dimensionless equations for charge and electric field	18
2.3.3	Reduction to an Ohmic regime	20
2.3.4	Charge equation: Ohm's law approximation	21
2.4	Boundary conditions	22
2.4.1	Electric stress	22
2.4.2	Boundary conditions on the fluid	22
2.4.3	Surface charge equation	23
<b>3</b>	<b>Computational Methods</b>	<b>25</b>
3.1	Implementation in Aria	25
3.2	CDFEM	28

3.3	Level set equations . . . . .	29
<b>4</b>	<b>Results</b>	<b>31</b>
4.1	Interfacial method comparison . . . . .	31
4.2	Verification . . . . .	32
4.2.1	Maxwell stress tensor verification: viscous flow due to charge . . . . .	32
4.2.2	Charge density verification: Relaxation on a spherical drop . . . . .	33
	Bulk charge . . . . .	33
	Surface charge . . . . .	34
	Voltage . . . . .	35
	Uniform initial charge . . . . .	37
4.3	Validation . . . . .	38
4.4	Droplet coalescence and cone formation . . . . .	40
<b>5</b>	<b>Conclusion</b>	<b>43</b>
	<b>References</b>	<b>44</b>
	<b>Appendix</b>	
A	The axisymmetric Maxwell stress tensor . . . . .	49
B	Summary of scales and constants . . . . .	50
C	Force comparisons . . . . .	51
D	Groupings . . . . .	52
E	Units associated to electric charge . . . . .	54

# List of Figures

1.1	A water droplet is placed into a column of immiscible silicon oil on top of salt water in the experimental apparatus shown on the left. An external electric field is applied. Due to electrophoresis, the drop initially moves upward toward the electrode, gains charge and then proceed downward toward the lower water surface. The magnitude of the applied electric field dictates whether the droplet merges or “bounces.” Past a critical electric field strength, the cone angle is sharp enough that, after initial contact and charge transfer, the droplet pinches off from the reservoir. Figure Courtesy of William Ristenpart [34]. . .	10
1.2	Formation of daughter droplets. Figure Courtesy of William Ristenpart [16]. .	11
3.1	Illustration of CDFEM in action for oppositely charged droplets merging under the influence of an electric field. . . . .	25
3.2	Illustration of CDFEM mesh cutting algorithm . . . . .	28
4.1	Simulations of a droplet falling due to gravity. Left Panel: ALE method, Center Panel: Diffuse level set method, Right Panel: CDFEM. . . . .	32
4.2	Verification study for Maxwell stress tensor: (Left) Velocity profile on $[0, 1] \times [0, 1]$ domain for $u(x, y) = 0.5xy^2$ . (Center) Slice through domain for all variable at $x = 0.75$ . (Right) Demonstrating second order accuracy of velocity profile with applied electrical force. Four meshes are analyzed (represented by solid squares). . . . .	34
4.3	Geometry for verification problem: two concentric spheres. The interior sphere is conductive and carries a charge. The outer sphere is an insulator. . .	35
4.4	Verification for charge density implementation: Left: Voltage potential comparison between analytic solution and computational solution. Right: Charge density decays appropriately, however for simple no-flux boundary conditions, charge at the interface remains constant or builds up much slower than it should if total charge were preserved. . . . .	38
4.5	Electrically driven partial coalescence, showing vortex penetration. The surrounding oil is highly viscous. The water droplet contains blue food dye for visualization of the penetrating vortex, which demonstrates that the fluid advection time scale should not be neglected. Figure courtesy of William Ristenpart [16]. . . . .	39

4.6	Simulation result for validation experiment to be compared with merging droplet and vortex formation in [16] and shown in Figure 4.5. ....	39
4.7	Simulation results for cone formation of a charged drop as it impacts an oppositely charged water surface. The aqueous bridge that forms is asymmetric, resulting from the mesh visibility at the neck width (about 5-10 elements wide).	40
4.8	3D charged droplet simulation. Blue color represents “dye injection” from droplet fluid into the lower water reservoir. ....	41

# Chapter 1

## Introduction

### 1.1 Applications and inspiration

Electric field induced droplet motion has developed quite a diverse range of applications including petroleum and vegetable oil dehydration [11], electrowetting (using electric fields to modify surface tension effects) [38], lab on a chip technology [10, 12], cloud formation [27], ink-jet printing [5], microfluidic devices for high-speed sorting [22], as well as electrospray dynamics and fuel atomization [1]. Precise control over droplets is crucial to many of these applications, however for most the physics are only partially understood. In addition, there are applications of interest to Sandia that may in the near future benefit from the use of electric fields to manipulate fluids and enhance or deter droplet coalescence, including nuclear waste reprocessing, purifying bio-diesel fuel, and solution separation for chemical detectors.

Recently, it has been demonstrated that high speed transport and separation of small particles against fluid flow in microfluidic devices can be accomplished using ratcheted electrophoresis [10]. State of the art *in vitro* designs for ultra-high throughput microfluidic devices for protein engineering and directed evolution have been developed using electric fields [12]. In fact, using electric fields to manipulate droplets in microfluidic channels has proven to be quite successful [40]. Precise manipulation of fluid droplets has aided in enabling new technologies for high-throughput reactors. Reactions for such devices only require minute amounts of reactants and are at high risk for contamination. Combining very small droplets can be hindered by surface tension and surfactant, however using electric fields to move droplets has the ability to overcome these obstacles by making coalescence more favorable since the conical tips are easily able to penetrate the lubrication layer. Containing reactants in charged droplets and using electric fields to manipulate their motion (and coalescence) can create highly efficient microfluidic reactors [22].

Electric fields can induce complex and unpredictable fluid dynamics. Oppositely charged water drops immersed in silicon oil experience attractive forces that would favor their coalescence. However, recent experiments with high speed cameras [34] demonstrate the counter-intuitive behavior that these oppositely charged droplets “bounce” rather than coalesce in the presence of strong electric fields (see Figure 1.1). High speed cameras show that a transient aqueous bridge forms between approaching drops prior to the non-coalescence repulsion event.

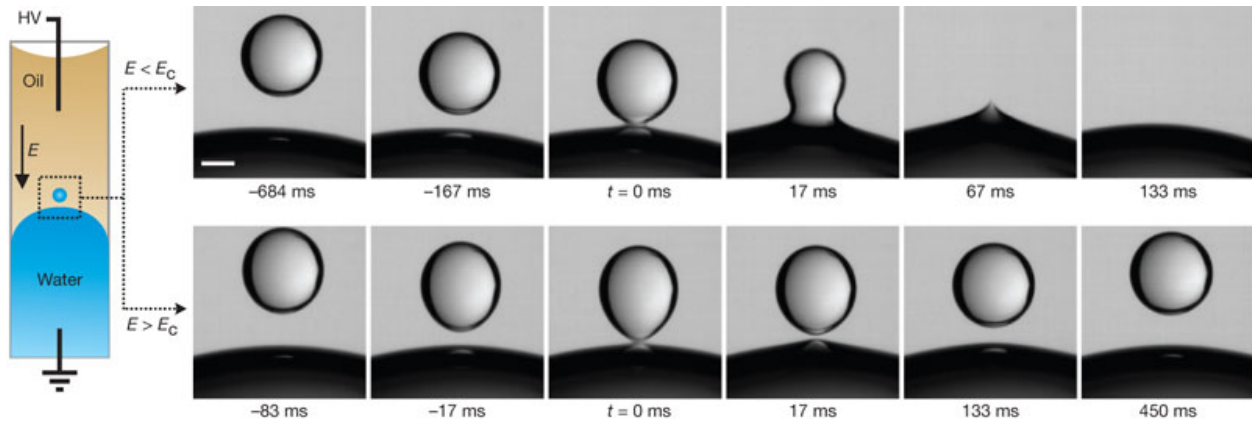


**Figure 1.1.** A water droplet is placed into a column of immiscible silicon oil on top of salt water in the experimental apparatus shown on the left. An external electric field is applied. Due to electrophoresis, the drop initially moves upward toward the electrode, gains charge and then proceed downward toward the lower water surface. The magnitude of the applied electric field dictates whether the droplet merges or “bounces.” Past a critical electric field strength, the cone angle is sharp enough that, after initial contact and charge transfer, the droplet pinches off from the reservoir. Figure Courtesy of William Ristenpart [34].

When exposed to an electric field, molecules in a water droplet will polarize and result in a net force on the droplet. There are also intermediate regimes in which the droplets partially coalesce and also regimes in which daughter droplets form (see Figure 1.2) [16]. The experiments in which this bouncing phenomenon is observed suggest that the electric field drives the formation of a meniscus bridge between approaching drops. This transient bridge may provide a small amount of charge transfer before destabilizing and could result in the observed bounce/pinch-off event. It is not well understood why this bifurcation between coalescence and pinch off occurs. This behavior does not appear to be due to inertial, Marangoni flow or Maxwell stresses. The observation of this non-coalescence event extends to many types of fluids, including vinegar in olive oil, ethanol in mineral oil and deionized water in air [34]. This indicates that the phenomenon is universal in nature and can occur for any liquid-liquid or liquid-gas system exposed to a strong electric field.

In a following paper [2] the explanation for non-coalescence is proposed as follows: the electric field primarily defines the shape of conical tips at contact, and upon contact capillary forces (which force fluid in or out of the neck region) determine whether or not the drops coalesce. Therefore shape - specifically curvature around the neck - is the determining factor to merging/pinch-off. The authors propose a theoretical model based on shape of bridge and capillary pressure. The experimental data contained in [2] agree reasonably well with

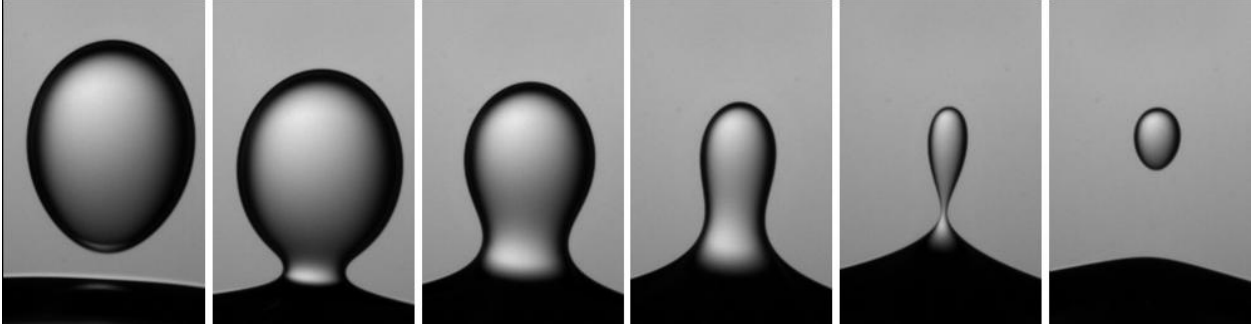


**Figure 1.2.** Formation of daughter droplets. Figure Courtesy of William Ristenpart [16].

theory, although the theoretical angle ( $31^\circ$ ) slightly over-predicts coalescence ( $28^\circ \pm 2^\circ$ ) provided in [34] and [2].

Another recent explanation contradicts the idea that instability due to surface tension and capillary pressure causes the aqueous bridge to pinch off [17]. They state that after charge transfer occurs (and the force pulling the droplets together disperses), the theory of mean curvature flow (minimizing the surface area) alone is enough to argue for the bouncing effect and suggest that the critical cone angle is slightly smaller. Therefore, they argue that geometry alone is enough to cause droplets to recoil and inertial effects should not be relevant. The critical cone angle in this work ( $24^\circ$ ) slightly under-predicts experimental observation.

The shape of the cone at which merging occurs in is somewhat universal in nature. For example, membrane junction assembly forms an adhesive cone with a surface deformation due to repulsion of the form  $u^{-3}$ , where  $u$  is displacement [4]. This form is due to the bending moment, but this  $u^{-3}$  power can also be derived from the surface tension effects [20]. Detailed analysis of surface tension driven merging of two identical wedged-shaped fluid regions has been performed where the wetting angle and shape of merging structures are found numerically for self-similar structures [19].

There are cases where naturally accumulated electric charge has been observed to cause Taylor cone droplet coalescence even without an externally applied electrical field [39]. The formation of cone-jets (a sub-set of Taylor cones) in charged liquids is well understood analytically for certain fluid regimes and assumptions [13]. Taylor cones form under the influence of strong electric fields that pull charged (and neutral) droplets to opposite poles, and can cause the formation of tiny daughter droplets at the tips (as in electro-sprays). These Taylor cones result from a balance between charge induced pressure from an electric field and capillary pressure. The electrocapillary number  $\xi_c = \frac{\epsilon\epsilon_0 r E^2}{\gamma}$ , where  $\epsilon\epsilon_0$  is the permittivity,  $r$  is the drop radius,  $E$  is the electric field, and  $\gamma$  is the surface tension provides a measure for this balance. Other types of Taylor cones, including the regime that is the focus of this manuscript, remain poorly understood. Unlike traditional Taylor cones, the conical

tips observed in these experiments have cone angles that are dependent on electrocapillary number [2].

## 1.2 Overview of numerical approaches

Accurately modeling moving interfaces is a challenging problem within itself, and an area currently under active investigation. There is a wide body of work for numerical methods of two-phase flows where the influence of an electric field is taken into account. In general, interface behavior is modeled by either interface-tracking (boundary integral, surface marker particles) or interface-capturing methods (volume-of-fluid, level set methods), each of which has its own set of advantages and disadvantages. The main distinction between these techniques is that interface-tracking methods track discrete points on the interface surface explicitly and interface-capturing methods evolve indicator functions that implicitly define the boundary. Interface-capturing methods have the advantage that the curvature and surface tension of the boundary can be easily calculated. However, these methods can suffer from unphysical mass loss or gain. Interface-tracking methods are able to accurately capture the interface without unphysical mass fluctuations, however one needs to add or remove surface-marker points in order to obtain sufficient interface resolution when stretching, coalescence and pinching occur. Interface-tracking methods are also subject to mesh tangling at high Reynolds number, but may be better suited for accurately defining coalescence without the fine spatial resolution necessary for an interface-capturing method near coalescence.

The volume of fluid (VOF) method has been successfully used to simulate deformation of two-phase flows exposed to electric fields [37]. One group presents a VOF charge conservation scheme that can handle a variety of electrohydrodynamic problems [23]. However, this method is not used to model coalescence or pinch-off, since one weakness of VOF is that it can not distinguish topological changes precisely. The current literature also includes a front-tracking finite volume method that can model electric charge on the droplet surface [18]. In addition, mesoscopic methods such as Lattice Boltzmann methods have been used for simulating drop deformation using electric fields [41, 14].

Recent work in the area of computational multi-phase flow modeling include hybrid Lagrangian-Eulerian particle-level set methods [21, 7] (to better handle the mass conservation problems inherent to level set methods) and moving mesh interface tracking method with local mesh adaptation [32, 31]. Robust adaptive re-meshing algorithms are necessary to handle topological changes for moving mesh methods [6]. Li *et al.* [21] used this hybrid method to model two-phase turbulent flow and were able to handle complex surface topologies. However, this method is used with finite difference schemes for structured meshes and we would like to take advantage of unstructured grids because they allow for more accurate interface representation. Quan *et al.* [31] were able to handle large deformations as well as interfacial breakup using mesh adaptation and separation, but had to balance unphysical mass loss or gain with computation time.

The Arbitrary Lagrangian-Eulerian (ALE) method [9] can be used in conjunction with a level set method to capture the interface [29]. This approach has been used for simulating droplet collisions. It has also been applied to electrically-induced deformations of water/oil interfaces [33]. Mesh distortion without degradation can be aided by the use of edge swapping and mesh smoothing for three-dimensional elements for large deformation problems [8]. However, topological changes have to be handled in an *ad hoc* careful fashion and get increasingly more complex in 3D. However, ways to handle topological changes in an automatic way using shape skeletons and distance functions to decide in the fly when topological changes occur are also in development [25].

The ghost fluid level set method is also a promising direction for modeling electrohydrodynamic multi-phase flows. This technique can handle droplet break-up and coalescence in a more natural way than moving mesh methods [3, 30]. However, charge transfer dynamics are neglected in both of these works: Bjørklund *et al.* [3] neglect charge completely and Van Poppel *et al.* [30] assume constant volumetric charge. This group most recently models two-phase electro-hydrodynamic flow for liquid fuel injection assuming a high electric Reynolds number. They use a ghost fluid-level set method for a multiphase fluid that handles discontinuities with generalized Taylor series expansions. This method is able to capture jumps in scalar values well, yet is lower order for capturing the correct fluid stress balance. For our purposes, we cannot make the same assumptions; viscous and Coulomb forces dominate during pinch off, but inertia is important for regimes where partial coalescence occurs, and dielectric forces are necessary during the formation of the meniscus bridge.

Accurate and stable interface-tracking methods capable of capturing and predicting coalescence and break-up of interfaces are currently a major challenge in the computational science community. Including electric forces and charge pose further challenges due to the complexity of electrostatic and hydrodynamic interactions involved in coalescence. Therefore, we require a novel modeling approach to understand this phenomenon. This project entails the creation of an interface-tracking model using the advantages of the Conformal Decomposition Finite Element Method (CDFEM) [24] with the capability to reproduce experiments, make predictions for future experiments and answer questions about the physics of this phenomenon that are not experimentally accessible. CDFEM treats interfacial dynamics by cutting elements along the boundary such that the interface is exactly aligned with element surfaces. This approach has many advantages including straightforward implementation of interfacial Dirichlet boundary conditions, zero interfacial thickness, the ability to handle complex topologies using unstructured meshes, and good convergence for stationary problems.



# Chapter 2

## Governing Equations

To describe the dynamics of a charged water drop immersed in silicon oil and exposed to an applied electric field, we need to solve the fluid equations of motion for mass and momentum, the electric field, and the charge density distribution. In this chapter we present our governing equations, boundary conditions and the assumptions made based on the physical scales of the problem apparatus.

### 2.1 Fluid equations

#### 2.1.1 Navier-Stokes equations

We utilize the incompressible Navier-Stokes equations for mass and momentum to govern both fluid phases:

$$\nabla \cdot \mathbf{u} = 0, \quad (2.1.1)$$

$$\rho \left( \frac{\partial \mathbf{u}}{\partial t} + \mathbf{u} \cdot \nabla \mathbf{u} \right) = -\nabla p + \nabla \cdot (\mathbf{T}^\mu + \mathbf{M}), \quad (2.1.2)$$

where  $\rho$  is the fluid density,  $\mathbf{u}$  is the velocity vector and  $p$  is the pressure. The viscous stress tensor,  $\mathbf{T}^\mu$ , is given by

$$\mathbf{T}^\mu = \mu(\nabla \mathbf{u} + \nabla \mathbf{u}^T), \quad (2.1.3)$$

where  $\mu$  is the fluid viscosity.  $\mathbf{M}$  represents the Maxwell stress tensor, the divergence of which is the force on the fluid due to an electric field. In order to compute this term, we need to consider the electromagnetic equations.

#### 2.1.2 Electric force in the momentum equation

The Maxwell stress tensor [15] is given by

$$\mathbf{M} = \varepsilon \left( \mathbf{E}\mathbf{E}^T - \frac{1}{2}(\mathbf{E} \cdot \mathbf{E})\mathbf{I} \right) \quad (2.1.4)$$

where  $\varepsilon$  is the electrical permittivity,  $\mathbf{E}$  is the electric field, and  $\mathbf{I}$  represents the identity tensor. The force on a fluid due to an electric field is given by the divergence of the Maxwell stress tensor:

$$\mathbf{F}_e = \nabla \cdot \mathbf{M} = \nabla \cdot (\varepsilon \mathbf{E} \mathbf{E}^T) - \frac{1}{2} \nabla (\varepsilon \mathbf{E} \cdot \mathbf{E}). \quad (2.1.5)$$

Using the identity

$$\nabla \cdot (\varepsilon \mathbf{E} \mathbf{E}^T) = (\nabla \cdot \varepsilon \mathbf{E}) \mathbf{E} + (\varepsilon \mathbf{E} \cdot \nabla) \mathbf{E}, \quad (2.1.6)$$

we can rewrite equation 2.1.5 as

$$\nabla \cdot \mathbf{M} = (\nabla \cdot \varepsilon \mathbf{E}) \mathbf{E} + (\varepsilon \mathbf{E} \cdot \nabla) \mathbf{E} - \frac{1}{2} \nabla (\varepsilon \mathbf{E} \cdot \mathbf{E}). \quad (2.1.7)$$

If the time scale for magnetic effects is sufficiently small,<sup>1</sup> then we can assume that  $\mathbf{E}$  is irrotational. Since the electric field is irrotational, it is also true that  $\mathbf{E} \times (\nabla \times \mathbf{E}) = 0$ , which implies that

$$\frac{1}{2} \nabla (\mathbf{E} \cdot \mathbf{E}) = \mathbf{E} \times (\nabla \times \mathbf{E}) + (\mathbf{E} \cdot \nabla) \mathbf{E} = (\mathbf{E} \cdot \nabla) \mathbf{E} \quad (2.1.8)$$

from a vector product rule identity. Also note that we can re-write the first term on the left-hand-side of equation 2.1.7 using the voltage equation (equation 2.2.1),

$$\nabla \cdot \varepsilon \mathbf{E} = \rho_v. \quad (2.1.9)$$

Thus, using equations 2.1.8 and 2.1.9, we can further simplify equation 2.1.7 to be

$$\mathbf{F}_e = \nabla \cdot \mathbf{M} = \rho_v \mathbf{E} + \frac{\varepsilon}{2} \nabla (\mathbf{E} \cdot \mathbf{E}) - \frac{1}{2} \nabla (\varepsilon \mathbf{E} \cdot \mathbf{E}) \quad (2.1.10)$$

$$\mathbf{F}_e = \nabla \cdot \mathbf{M} = \rho_v \mathbf{E} + \frac{\varepsilon}{2} \nabla (\mathbf{E} \cdot \mathbf{E}) - \frac{\varepsilon}{2} \nabla (\mathbf{E} \cdot \mathbf{E}) - \frac{1}{2} (\mathbf{E} \cdot \mathbf{E}) \nabla \varepsilon \quad (2.1.11)$$

$$\mathbf{F}_e = \nabla \cdot \mathbf{M} = \rho_v \mathbf{E} - \frac{1}{2} (\mathbf{E} \cdot \mathbf{E}) \nabla \varepsilon. \quad (2.1.12)$$

This clearly shows that the electric forcing term in the Navier-Stokes equation,  $\mathbf{F}_e$ , is non-zero if there is an electric field and a charge in the bulk or spatially varying electric permittivity. For the purpose of the electro-coalescence problem, the second term will only apply at an interface since  $\varepsilon$  is assumed to be constant within a given medium (water or silicon oil).

### 2.1.3 Magnetic versus electric time scales

The characteristic time scale for magnetic phenomena is  $t_m = \mu_m \sigma L^2$ , where  $\mu_m$  is the magnetic permeability,  $\sigma$  is the conductivity and  $L$  is a length scale. We can safely assume that magnetic effects are small enough to be ignored if this time scale is considerably smaller than the electric time-scale,  $t_e = \varepsilon / \sigma$  [36].

---

<sup>1</sup>Magnetic effects can be ignored for most electrohydrodynamic flows. For a more detailed analysis see Section 2.1.3

We consider a system involving salt water in poorly conducting silicon oil. As such the electric time scale,  $\tau_e$  will be determined by the water, which has as relative permittivity of  $\tilde{\varepsilon} \approx 80$ . Using the permittivity of free space  $\varepsilon_0 = 8.85 \times 10^{-12}$  F/m, the effective permittivity of water is  $\varepsilon = \tilde{\varepsilon}\varepsilon_0 = 7 \times 10^{-10}$  F/m. In experiments conducted by Ristenpart *et al.* [34], the conductivity of water is varied by adding salt (KCl), and is bounded as  $4 \times 10^{-4}$  S/m  $\leq \sigma \leq 2 \times 10^{-2}$  S/m. Thus the electric time scale is bounded by

$$4 \times 10^{-8} \text{s} \leq \tau_e \leq 2 \times 10^{-6} \text{s}.$$

With a magnetic permeability of  $\mu_m = 10^{-6}$  H/m [23], the characteristic timescale of magnetic forces is given by

$$\tau_m = \mu\mu_0\sigma R_0^2, \quad (2.1.13)$$

where the drop radius,  $R_0 \approx 1$  mm, is used as a characteristic length scale. Therefore, applying these parameters, we can conclude that

$$\tau_m \leq 2 \times 10^{-14} \text{s} \ll \tau_e$$

and safely neglect magnetic forces.

## 2.2 The voltage equation

The voltage equation (shown here in terms of the electric field  $\mathbf{E} = -\nabla\phi$  since we assume  $\mathbf{E}$  is irrotational),

$$-\nabla \cdot (\varepsilon \nabla \phi) = \nabla \cdot (\varepsilon \mathbf{E}) = \rho_V, \quad (2.2.1)$$

describes how the electric field is affected by the bulk charge density  $\rho_V$ . If we allow for charge to accumulate at the interface, the jump in the electric field across the interface can be written in terms of the charge per unit area,  $q$ :

$$\|\varepsilon \mathbf{E}\| \cdot \mathbf{n} = q, \quad (2.2.2)$$

where  $\mathbf{n}$  is the unit vector normal to the surface,  $q$  represents the surface charge, and  $\|\cdot\|$  represents the jump across an interface.

## 2.3 Charge distribution

### 2.3.1 Charged species

In general, the electric charge density,  $\rho_V$ , is the sum of ionic species concentrations. In particular, the relation

$$\rho_V = \sum_k e z^k n^k \quad (2.3.1)$$

where  $e$  is an elementary unit of charge of a proton,  $n^k$  is the density of a particular species,  $z^k$  and is the valence of the  $k$ th species. Let  $\omega^k$  be the migration velocity associated with species  $k$ . The species conservation equation can be written as

$$\frac{\partial n^k}{\partial t} + \mathbf{u} \cdot \nabla n^k = \nabla \cdot \left( -\omega^k e z^k n^k \mathbf{E} + \omega^k k_B T \nabla n^k \right) + r^k \quad (2.3.2)$$

where  $k_B$  is the Boltzmann constant and  $T$  is the temperature [36]. The term  $-\omega^k e z^k n^k \mathbf{E}$  represents migration due to electric forces, the term  $\omega^k k_B T \nabla n^k$  accounts for species diffusion, and  $r^k$  is a source term based on chemical reactions between species.

For the case of a strong electrolyte such as potassium chloride (KCl) dissolved in water, we can neglect a neutral species, and ignore chemical reactions. We account for two species: a positive species,  $\text{K}^+$ , and a negative species,  $\text{Cl}^-$ . Thus in terms of ionic concentrations, the voltage equation becomes

$$\nabla \cdot (\varepsilon \varepsilon_0 \mathbf{E}) = e(n^+ - n^-) \quad (2.3.3)$$

and the two species conservation equations are

$$\frac{\partial n^k}{\partial t} + \mathbf{u} \cdot \nabla n^k = \nabla \cdot \left( -\omega^k e z^k n^k \mathbf{E} + \omega^k k_B T \nabla n^k \right) \quad (2.3.4)$$

for  $k = +, -$ . We can write an advection equation for the electric charge density by summing up the species conservation equations multiplied by their valences and elementary unit charge (using the definition of  $\rho_V$  in equation 2.3.1),

$$\frac{\partial \rho_V}{\partial t} + \mathbf{u} \cdot \nabla \rho_V = \nabla \cdot \left( \sum_k (-\omega^k e^2 n^k \mathbf{E}) + \omega^k k_B T \nabla \rho_V \right). \quad (2.3.5)$$

To solve this equation for charge density, we still need information about each species. We would like a form of this equation in which we only need to track charge density and the electric field. In order to do so, we first perform a scaling analysis.

## 2.3.2 Dimensionless equations for charge and electric field

Given that the experiments we are attempting to simulate [34] use an applied electric field magnitude within the range  $10^5 \text{V/m} \leq E_0 \leq 10^6 \text{V/m}$ , this gives us a natural scale for the electric field:  $\mathbf{E} \rightarrow \mathbf{E}/E_0$ . We assume oil is a dielectric containing no mobile ions. Then charge need only be tracked in the water phase. As stated previously, the relative permittivity of water is  $\varepsilon_w \approx 80$ . We scale the Maxwell stress tensor by an electric pressure:  $\mathbf{T}^e \rightarrow \mathbf{T}^e/E_0^2 \varepsilon_w \varepsilon_0$  where

$$\varepsilon_w \varepsilon_0 E_0^2 = (80)(8.854 \times 10^{-12} \text{F/m})(3 \times 10^5 \text{V/m})^2 \approx 63.74 \text{Pa}. \quad (2.3.6)$$

At room temperature ( $T = 300 \text{K}$ ), the ion diffusivities of potassium and chloride are  $\omega(\text{K}^+)k_B T \approx 2.65 \times 10^{-9} \text{m}^2/\text{s}$  and  $\omega(\text{Cl}^-)k_B \approx 1.70 \times 10^{-9} \text{m}^2/\text{s}$ ; respectively, where  $k_B \approx$

$1.38 \times 10^{-23} \text{J/K}$  is the Boltzmann constant. Their respective ion mobilities are  $e\omega(\text{K}^+) \approx 7.15 \times 10^{-8} \text{m}^2/\text{V s}$  and  $e\omega(\text{Cl}^-) \approx 6.85 \times 10^{-8} \text{m}^2/\text{V s}$ , where  $e \approx 1.6 \times 10^{-19} \text{C}$  is an elementary charge. This gives a natural scale for the ion mobility of  $\omega_0 = \omega(\text{K}^+) + \omega(\text{Cl}^-)$ . If a total of  $0.2 \text{mM KCl} = 0.2 \text{mol/m}^3 \text{KCl}$  is injected into the drop, this gives rise to a charge density of approximately

$$en_0 \approx (1.6 \times 10^{-19} \text{C})(0.2 \text{mol/m}^3 \text{KCl})(6 \times 10^{23} / \text{mol}) \approx 2 \times 10^4 \text{C/m}^3.$$

With these values, we can estimate the conductivity of the solution to be

$$\sigma \approx e^2 n_0 \omega_0 \approx 32 \times 10^{-4} \text{S/m}.$$

In their experiments, Ristenpart *et al.* [34] controlled the conductivity by varying the concentration of KCl in the water droplet, obtaining a range of

$$4 \times 10^{-4} \text{S/m} \leq \sigma \leq 164 \times 10^{-4} \text{S/m}.$$

Using this range of values, we rescale the ion density  $n^\pm \rightarrow n^\pm/n_0$ , the ion mobility  $\omega^\pm \rightarrow \omega^\pm/\omega_0$ , and the charge density  $\rho_V \rightarrow \rho_V/en_0$ .

Assuming constant permittivity, the voltage equation,

$$\nabla \cdot \mathbf{E} = \text{Ch}_i \rho_V, \quad (2.3.7)$$

can be written in dimensionless form using an ion charge number

$$\text{Ch}_i = \frac{en_0 R_0}{\varepsilon_w \varepsilon_0 E_0} \sim \frac{(2 \times 10^4 \text{C/m}^3)(10^{-3} \text{m})}{(80)(8.854 \times 10^{-12} \text{F/m})(3 \times 10^5 \text{V/m})} \approx 10^5. \quad (2.3.8)$$

The species conservation equations can now be written in terms of dimensionless variables (denoted as  $a = a_0 \tilde{a}$ ) as

$$\frac{n_0}{\tau} \frac{\partial \tilde{n}^k}{\partial \tilde{t}} + \tilde{\mathbf{u}} \cdot \tilde{\nabla} \tilde{n}^k = \tilde{\nabla} \cdot \left( - \left( \frac{e\omega_0 n_0 E_0}{R_0} \right) \tilde{w}^k z^k \tilde{n}^k \tilde{\mathbf{E}} + \left( \frac{\omega_0 k_B T n_0}{R_0^2} \right) \tilde{w}^k \tilde{\nabla} \tilde{n}^k \right), \quad (2.3.9)$$

where  $\tau$  is a process timescale. We can divide this equation by the coefficient  $e\omega_0 n_0 E_0 / R_0$  from the electric forcing term to obtain a dimensionless bulk species conservation equation (and remove  $\tilde{a}$  on dimensionless variables for simplicity):

$$\frac{\tau_i}{\tau} \frac{\partial n^k}{\partial t} + \text{IoPe}_i \mathbf{u} \cdot \nabla n^k = \nabla \cdot \left( -\omega^k z^k n^k \mathbf{E} + \text{Io} \omega^k \nabla n^k \right) \quad \text{for } k = +, -. \quad (2.3.10)$$

We define the ion drift number to be

$$\text{Io} = \frac{k_B T}{e R_0 E_0} \approx \frac{4.14 \times 10^{-21} \text{J}}{(1.6 \times 10^{-19} \text{C})(10^{-3} \text{m})(3 \times 10^5 \text{V/m})} \approx 8.625 \times 10^{-5}, \quad (2.3.11)$$

the ion Peclet number as

$$\text{Pe}_i = \frac{R_0^2}{\omega_0 k_B T \tau}, \quad (2.3.12)$$

and the ion drift time scale

$$\tau_i = \frac{R_0}{eE_0\omega_0} \approx \frac{10^{-3}\text{m}}{(7.15 \times 10^{-8}\text{m}^2/\text{V s})(3 \times 10^5\text{V/m})} \approx 5 \times 10^{-2}\text{s}. \quad (2.3.13)$$

The corresponding charge density equation (by summation) is

$$\frac{\tau_i}{\tau} \frac{\partial \rho_V}{\partial t} + \text{IoPe}_i \mathbf{u} \cdot \nabla \rho_V = \nabla \cdot \left( \sum_k -\omega^k n^k \mathbf{E} + \text{Io} \omega^k \nabla \rho_V \right). \quad (2.3.14)$$

### 2.3.3 Reduction to an Ohmic regime

For this problem two scales are important: (1) The scale which is suitable for the dynamics before and after merging and (2) the scale of formation for an aqueous bridge. We choose the drop radius,  $R_0 \approx 1$  mm as a representative length scale and use a timescale,  $\tau$ , which will be determined later. Let  $t \rightarrow t/\tau$ ,  $\nabla \rightarrow R_0 \nabla$ ,  $\kappa \rightarrow R_0 \kappa$ , and  $\mathbf{u} \rightarrow \tau \mathbf{u}/R_0$ . Important dynamics occur on the smaller timescale of  $\tau_b = 10^{-5}$ s and length scale of  $R_b = 10^{-2}$ mm. Define  $\eta = \tau_b/\tau$  and  $\zeta = R_b/R_0 = 10^{-2}$ . Then the velocity, time, stress, curvature, and differential operators rescale to values relevant during merging, with a subscript of  $b$  denoting terms associated to the aqueous bridge:

$$t = \eta t_b \quad \nabla = \frac{\nabla_b}{\zeta} \quad \kappa = \frac{\kappa_b}{\zeta} \quad \mathbf{u} = \frac{\zeta}{\eta} \mathbf{u}_b$$

We can neglect ionic mobility since the ionic drift number is small  $\text{Io} \ll 1$  and therefore, equation 2.3.14 reduces to the charge density equation

$$\frac{\tau_i}{\tau} \frac{\partial \rho_V}{\partial t} + \text{IoPe}_i \mathbf{u} \cdot \nabla \rho_V = -\nabla \cdot (\sigma \mathbf{E}) \quad (2.3.15)$$

where we have defined a dimensionless ohmic conductivity

$$\sigma = \sum_k \omega^k n^k. \quad (2.3.16)$$

We define a conduction time,  $\tau_e = \tau_i/\text{Ch}_i = \varepsilon_w \varepsilon_0 / \sigma_0$ , to obtain a reduced dimensionless equation for charge density,

$$\frac{D\rho_V}{Dt} = -\frac{\tau}{\tau_e} \rho_V \quad (2.3.17)$$

Since all timescales we consider are much larger than  $\tau_e \approx 10^{-7}$ s, the charge decay process will be relatively rapid, and we can assume there is no bulk charge in the water droplet, only charge at the surface. By neglecting ion mobility we can write the surface charge equation:

$$\frac{\tau_i}{\tau} \frac{\partial q}{\partial t} + \text{IoPe}_i (\mathbf{u} \cdot \nabla_s q + \mathbf{u} \cdot \mathbf{n} (\mathbf{n} \cdot \nabla) q) = -\|\sigma \mathbf{E}\| \cdot \mathbf{n}. \quad (2.3.18)$$

### 2.3.4 Charge equation: Ohm's law approximation

The charge density equation

$$\frac{\partial \rho_V}{\partial t} = \nabla \cdot \mathbf{J} = \nabla \cdot (-\sigma \mathbf{E} + \rho_V \mathbf{u}) \quad (2.3.19)$$

is a conservation equation for the bulk free charge, where  $\mathbf{J}$  as the flux of electric charge. Here we choose Ohm's law  $-\sigma \mathbf{E}$ , with  $\sigma$  as the conductivity of the medium, to govern how the charged 'particles' are affected by the electric field. More detailed models exist, such as Nerst-Planck, in which individual ionic species get tracked via advection-diffusion-reaction equations with additional terms involving the influence of the electrical field on charged particles (see equations 8-22 of [36] for further detail).

In the absence of fluid motion (fluid velocity is zero:  $\mathbf{u} = 0$ ), the voltage equation can be used to simplify the charge density equation, written only in terms of the charge density,

$$\frac{\partial \rho_V}{\partial t} = -\frac{\sigma}{\epsilon} \rho_V \quad (2.3.20)$$

This relation implies that charge decays in the bulk media. The greater the conductivity, the faster this decay occurs. In fact, in a perfect conductor, the electric field is zero.

Charge density equation

$$\frac{\partial \rho_e}{\partial t} = \nabla \cdot \mathbf{J} = \nabla \cdot (-\sigma \mathbf{E} + \rho_e \mathbf{u}) \quad (2.3.21)$$

In the absence of fluid motion we can use the voltage equation to simplify this relation to be only in terms of  $\rho_e$

$$\frac{\partial \rho_e}{\partial t} = -\frac{\sigma}{\epsilon} \rho_e \quad (2.3.22)$$

since  $\epsilon \nabla \cdot \mathbf{E} = \rho_e$ . Charge decays in the bulk media in an conductor and for longer times scales only exists on the surface. The charge density equation for the bulk is different for slow conduction, in which the typical assumption is that charge only exists on the surface or interface.

Although the Ohmic regime applies to the drop length scale, it is unclear whether it applies to the smaller scale associated with merging. Rescaling our dimensionless equations, we get

$$\nabla_b \cdot \mathbf{E} = \zeta \text{Ch}_i \rho_V \quad (2.3.23)$$

$$\frac{\zeta^2}{\eta} \left( \frac{\tau}{\tau_i} \frac{\partial n^k}{\partial t_b} + \text{IoPe}_i \mathbf{u}_b \cdot \nabla_b n^k \right) = \nabla_b \cdot (-\zeta \omega^k z^k n^k \mathbf{E} + \text{Io} \omega^k \nabla_b n^k) \quad (2.3.24)$$

This leads to a charge conservation equation of

$$\frac{\zeta^2}{\eta} \frac{\tau}{\tau_i} \frac{d\rho_V}{dt_b} = -\zeta \nabla_b \sigma \cdot \mathbf{E} - \zeta^2 \text{Ch}_i \sigma \rho_V + \text{Io} \nabla_b^2 (\omega^+ n^+ - \omega^- n^-)$$

Here, the term involving the conductivity gradient is scaled by  $\zeta \sim 10^{-2}$ ; the Ohmic term is scaled by a factor of  $\zeta^2 \text{Ch}_i \sim 10^1$ ; and the ion mobility is scaled by the ion drift number:  $\text{Io} \sim 10^{-4}$ . The Ohmic term is dominant by about three orders of magnitude, so we conclude that the other two terms can be neglected, and we again find ourselves in the Ohmic regime.

## 2.4 Boundary conditions

The boundary conditions for this model include how velocity and pressure are handled at the interface as well as the voltage and the electric charge.

### 2.4.1 Electric stress

The electric field can be decomposed into normal and tangential components, to find

$$\mathbf{E} \cdot \mathbf{E} = E_n^2 + E_{t_1}^2 + E_{t_2}^2.$$

We can also compute the Maxwell stress acting normal to the interface:

$$\mathbf{M} \cdot \mathbf{n} = \varepsilon\varepsilon_0 \left( E_n \mathbf{E} - \frac{1}{2} E^2 \mathbf{n} \right).$$

which gives the jump in stress as

$$\|\mathbf{M} \cdot \mathbf{n}\| = \|\varepsilon\varepsilon_0 E_n \mathbf{E}\| - \frac{1}{2} \|\varepsilon\varepsilon_0 E^2 \mathbf{n}\|.$$

The tangential stress jump across the interface is

$$\|\mathbf{M} \cdot \mathbf{n}\| \cdot \mathbf{t}_i = \|\varepsilon\varepsilon_0 E_n E_{t_i}\|.$$

The tangential electric field is continuous across the interface, so  $E_{t_i}$  can be removed from the above equation, to get

$$\|\mathbf{M} \cdot \mathbf{n}\| \cdot \mathbf{t}_i = \|\varepsilon\varepsilon_0 E_n\| \mathbf{E} \cdot \mathbf{t}_i = q \mathbf{E} \cdot \mathbf{t}_i.$$

In contrast, the normal jump across the interface is given by

$$\begin{aligned} \|\mathbf{M} \cdot \mathbf{n}\| \cdot \mathbf{n} &= \|\varepsilon\varepsilon_0 E_n^2\| - \frac{1}{2} \|\varepsilon\varepsilon_0 E^2\| \\ &= \|\varepsilon\varepsilon_0 E_n^2\| - \frac{1}{2} \|\varepsilon\varepsilon_0 E_n^2\| - \frac{1}{2} \|\varepsilon\varepsilon_0 E_{t_1}^2\| - \frac{1}{2} \|\varepsilon\varepsilon_0 E_{t_2}^2\| \\ &= \frac{1}{2} \|\varepsilon\varepsilon_0 (E_n^2 - E_{t_1}^2 - E_{t_2}^2)\|. \end{aligned}$$

### 2.4.2 Boundary conditions on the fluid

In the absence of electric forces and fluid motion, the Young-Laplace equation gives the interfacial pressure jump:

$$\|p\| = \gamma\kappa, \tag{2.4.1}$$

where  $\gamma$  is the surface tension, and  $\kappa$  is twice the mean curvature. Assuming a uniform surface tension, there is no change in the tangential stress across the interface:

$$\|\mathbf{T}^\mu \cdot \mathbf{n}\| \cdot \mathbf{t}_i = \mathbf{0} \quad (2.4.2)$$

$$\rho \frac{D\mathbf{u}}{Dt} = -\nabla P + \nabla \cdot (\mathbf{T}^\mu + \mathbf{M}) - g(\rho - \rho_u) \mathbf{k} + \delta_s \gamma \kappa \mathbf{n} \quad (2.4.3)$$

Now integrate across the interface normally from a point  $\mathbf{x}_i$  to a point  $\mathbf{x}_e$  which are an infinitesimal distance  $\delta\ell$  from one another, recalling that the velocity is continuous across the interface:

$$\|\rho\| \frac{D\mathbf{u}}{Dt} \cdot \mathbf{n} \delta\ell = -\|p\| + \int_i^e \nabla \cdot (\mathbf{T}^\mu + \mathbf{M}) \cdot \mathbf{n} dl - g \|\rho\| \mathbf{k} \cdot \mathbf{n} \delta\ell + \int_i^e \delta_s \gamma \kappa \mathbf{n} \cdot \mathbf{n} dl. \quad (2.4.4)$$

The surface tension term is evaluated using the delta function:

$$\int_i^e \delta_s \gamma \kappa \mathbf{n} \cdot \mathbf{n} dl = \gamma \int_i^e \delta_s \kappa dl = \gamma \kappa. \quad (2.4.5)$$

The influence of the viscous and Maxwell stresses can be integrated using the Divergence Theorem:

$$\int_i^e \nabla \cdot (\mathbf{T}^\mu + \mathbf{M}) \cdot \mathbf{n} dl = \|(\mathbf{T}^\mu + \mathbf{M}) \cdot \mathbf{n}\| \cdot \mathbf{n}. \quad (2.4.6)$$

Evaluate the jump in viscous stress using continuity of velocity across the interface:

$$\|\mathbf{T}^\mu \cdot \mathbf{n}\| \cdot \mathbf{n} = \|\mu(\nabla \mathbf{u} + \nabla \mathbf{u}^T) \cdot \mathbf{n}\| \cdot \mathbf{n} = 2 \|\mu\| \left. \frac{\partial u_n}{\partial \ell} \right|_s. \quad (2.4.7)$$

Putting everything together and taking the limit as  $\delta\ell \rightarrow 0$ , we get the jump condition for momentum

$$\|p\| = \gamma \kappa + 2 \|\mu\| \left. \frac{\partial u_n}{\partial \ell} \right|_s + \frac{1}{2} \|\varepsilon \varepsilon_0 (E_n^2 - E_{t_1}^2 - E_{t_2}^2)\|. \quad (2.4.8)$$

### 2.4.3 Surface charge equation

Integrating the voltage equation 2.2.1 along an interface gives rise to the following boundary condition on voltage:

$$\|\varepsilon \varepsilon_0 \mathbf{E}\| \cdot \mathbf{n} = q \quad (2.4.9)$$

where  $q$  is defined as the surface charge. To obtain charge conservation at the interface, we integrate the charge density equation across the surface to get a surface charge equation [36], a PDE for  $q$ ,

$$\frac{\partial q}{\partial t} + \mathbf{u} \cdot \nabla_s q - q \mathbf{n} \cdot (\mathbf{n} \cdot \nabla) \cdot \mathbf{u} = -\|\sigma \mathbf{E} \cdot \mathbf{n}\| \quad (2.4.10)$$

where  $\nabla_s = (\boldsymbol{\delta} - \mathbf{n}\mathbf{n}) \cdot \nabla$  is the tangential gradient at the surface. The surface charge equations allows charge to accumulate at the interface and advect with the tangential velocity along the interface. The diffusion term is neglected here, as consistent with the bulk charge density equation.



# Chapter 3

## Computational Methods

The method described in this report has been implemented in the Aria module within Sierra [26]. The Conformal Decomposition Finite Element Method (CDFEM) [24] is used to capture the interfacial dynamics using the Krino module of Sierra for the level set and conformal mesh functionality. This work is the first to use CDFEM to model multi-phase electrohydrodynamic flows (see Figure 3.1).

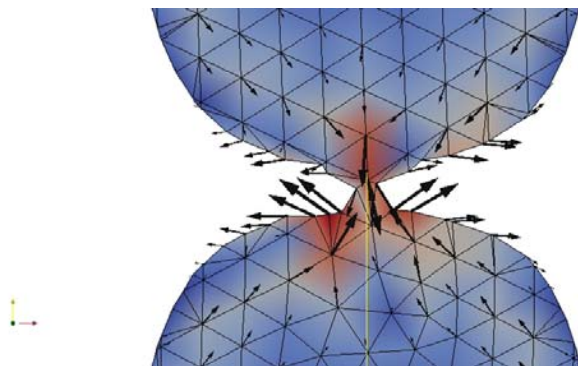


**Figure 3.1.** Illustration of CDFEM in action for oppositely charged droplets merging under the influence of an electric field.

### 3.1 Implementation in Aria

The force on the fluid due to the electric field gets added to the momentum equation with this line:

```
Momentum Stress = Maxwell
```

is included in the material block of the input file. In Aria, the Maxwell momentum stress tensor gets added to the total stress tensor (including typically a form of the viscous stress tensor) and requires the charge density to be defined.

The voltage equation gets solved in Aria using the following input file syntax:

```
EQ Voltage for Voltage ON block_1 USING Q1 WITH DIFF SRC
Source For Voltage On block_1=Polynomial variable=CHARGE_DENSITY order=1 c0=0 c1=1
```

The term ‘DIFF’ activates the diffusion term ( $\nabla \cdot (\varepsilon \nabla \phi)$ ) and the ‘SRC’ term activates the source term, which is given explicitly in the second line as the charge density,  $c_0 + c_1 \rho_V = \text{SRC}$ . The Galerkin FEM residual for the voltage equation 2.2.1 in SIERRA/Aria is

$$R^i = \int_V (\nabla \cdot (\varepsilon \mathbf{E}) - \rho_V) \phi^i dV \quad (3.1.1)$$

$$R^i = - \int_V [(\varepsilon \mathbf{E}) \cdot \nabla \phi^i + \rho_V \phi^i] dV + \int_S \phi^i (\varepsilon \mathbf{E}) \cdot \mathbf{n} dS. \quad (3.1.2)$$

$$(3.1.3)$$

The charge density equation gets solved in Aria using the following input file syntax:

```
EQ Charge_Density for Charge_Density ON block_1 USING Q1 WITH MASS DIFF ADV SUPG
```

where the ‘MASS,’ ‘DIFF’ and ‘ADV’ terms are for the time derivative, Ohm’s law, and advection terms respectively. The ‘SUPG’ term activates an SUPG stabilization for advection dominated problems.

The Galerkin FEM residual for the charge density equation is

$$R^i = \int_V \left( \frac{\partial \rho_V}{\partial t} + \nabla \cdot (\sigma \mathbf{E} - \rho_V \mathbf{u}) \right) \phi^i dV \quad (3.1.4)$$

$$R^i = \int_V \left[ \left( \frac{\partial \rho_V}{\partial t} + \mathbf{u} \rho_V \right) \phi^i - (\sigma \mathbf{E}) \cdot \nabla \phi^i \right] dV + \int_S \phi^i (\sigma \mathbf{E}) \cdot \mathbf{n} dS. \quad (3.1.5)$$

$$(3.1.6)$$

Note that the natural boundary condition that falls out of the residual equation for charge density is  $\|\sigma \mathbf{E} \cdot \mathbf{n}\| = 0$ . Note that this equation could be written only in terms of  $\rho_V$  by substituting in the voltage equation to remove the electric field dependence and resulting in a advection-decay equation for the charge density. This form is avoided here due to the fact that one loses the coupling between these equations and it is no longer possible to put in a no-flux charge boundary condition in the ODE form. For this reason, the charge density equation is implemented with the original form in terms of the electric field. However, since it is  $\rho_V$  and not  $\mathbf{E}$  that is being solved for in this equation, the surface contribution of equation 3.1.6 needs to be explicitly included into the Aria input file in order to include the boundary term into the residual form for the charge density equation. This is done with the input file line:

BC Flux for Charge\_Density on oil\_BC = Nat\_E

Because of the integration by parts in equation 3.1.3, the natural boundary condition (also the default in Aria) is a no-flux boundary condition for  $\|\varepsilon\mathbf{E} \cdot \mathbf{n}\| = 0$  where  $\|\cdot\|$  represents the jump across the interface. Taking into account the fact that for our two-fluid problem there may be discontinuities in both material parameters  $\varepsilon$  and  $\sigma$  across the interface, this natural boundary condition is not equivalent to (and is in fact inconsistent with) no-flux of charge across the interface,  $\|\mathbf{J} \cdot \mathbf{n}\| = \|(-\sigma\mathbf{E} + \rho_V\mathbf{u}) \cdot \mathbf{n}\| \neq 0$ . A no-flux charge boundary condition across an interface between two immiscible fluids (one being conductive ionized water and the other being insulating silicon oil) makes the more sense as an interfacial boundary condition than the default boundary condition in this context.

For many relevant fluid time scales, charge only exists at the surface between conductors and insulators (where a no-flux boundary condition might be imposed at the interface  $\mathbf{J} \cdot \mathbf{n} = 0$  between a conductor and an insulator).

In order to impose a no-flux boundary condition at the interface, we can applying the corresponding flux to the voltage equation, such that  $\|(-\sigma\mathbf{E} + \rho_V\mathbf{u}) \cdot \mathbf{n}\| = 0$ . This is implemented as a user subroutine with the equation

$$\int_S \phi^i (\varepsilon\mathbf{E}) \cdot \mathbf{n} dS = \varepsilon_1 \mathbf{E}_{1,\mathbf{n}} - \varepsilon_2 \mathbf{E}_{2,\mathbf{n}}, \quad (3.1.7)$$

where

$$\mathbf{E}_{2,\mathbf{n}} = \frac{1}{\sigma_2} (\sigma_1 \mathbf{E}_{1,\mathbf{n}} + \rho_{V,1} \mathbf{u}_{\mathbf{n}}). \quad (3.1.8)$$

Here we make the assumption that charge density is only non-zero in the conductor, so that the  $\rho_{V,2}\mathbf{u}$  term drops out of one side of the equation. It is assumed that the velocity is continuous across the interface and therefore has no sub-index. This boundary condition can be invoked with the input deck syntax:

BC Flux for Voltage on surface\_1=Surface\_Charge e\_1=1.0e-11 s\_1=1.0e-12

Alternatively, we could instead allow charge to build up at the interface and have a governing equation of interfacial charge on shell elements between volume blocks of the mesh. A shell method for the lubrication equation has been successfully implemented in GOMA and Aria [35]. We track a surface charge equation at the interface that conserves charge and provides the boundary condition for the voltage equation at an interface [36]

$$q = \|\varepsilon\mathbf{E} \cdot \mathbf{n}\| \quad (3.1.9)$$

$$\frac{\partial q}{\partial t} = \mathbf{u} \cdot \nabla_s q - q\mathbf{n} \cdot (\mathbf{n} \cdot \nabla) \cdot \mathbf{u} + \|\sigma\mathbf{E} \cdot \mathbf{n}\| \quad (3.1.10)$$

where  $\nabla_s = (\mathbf{I} - \mathbf{nn}^T) \cdot \nabla$  is the surface gradient. Note that when there is no fluid flow ( $\mathbf{u} = 0$ ), the surface accrues charge due to an inward flux from the bulk medium. The input file syntax for the surface charge equation is:

Note that the surface charge equation is only applicable on shell elements and is still a research code and is not yet available in the master branch of Aria.

## 3.2 CDFEM

The conformal decomposition finite element method (CDFEM) [24] is a sharp interface method that decomposes elements along fluid-fluid boundaries and uses a level set function to represent the interface. By dynamically inserting nodes and edges as the interface evolves, weak and strong discontinuities can be described using standard finite element shape functions. This method is a generalization of the finite element method that adds nodes to unstructured meshes of triangles (in 2D, see Figure 3.2) and tetrahedra (in 3D). CDFEM

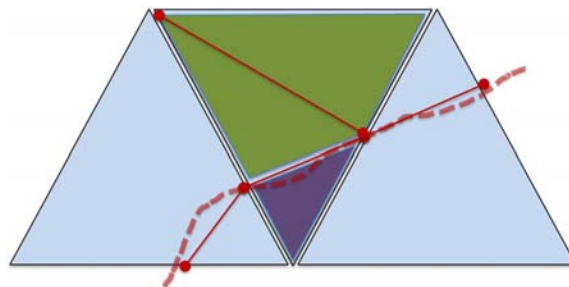


**Figure 3.2.** Illustration of CDFEM mesh cutting algorithm

allows the level set surface to arbitrarily cut through the original mesh, and therefore the quality of the resulting conformal elements could be in jeopardy since it can produce sliver elements. In [24], the method's accuracy is quantified and determined that optimal convergence rates for piecewise linear elements can be obtained both on the volumes and the surfaces containing the discontinuities. One can also compare CDFEM to the eXtended finite element method (XFEM) with Heaviside enrichment, since the XFEM space can be recovered by adding constraints on the nodes added in the conformal decomposition. In fact Noble *et al.* [24] found that CDFEM is no less accurate than XFEM with Heaviside enrichment.

A level set field is used to decompose the mesh, thus enriching the finite element description. This decomposition produces a standard set of elements which are then assembled using standard finite element shape functions and quadrature. This is in contrast to XFEM where interpolation and quadrature must be significantly modified to accommodate the enrichment. In CDFEM, element enrichment occurs by decomposing finite elements that span the zero level set into elements that conform to the original element as well as the zero level set surface. The level set field consists of a piecewise linear field on triangular (or in

3D, tetrahedral) elements. For dynamic meshes, elements are both added and removed as the interface evolves. Parent elements get subdivided into new sub-elements and nodes get added at interface intersection locations, but no Steiner points are created, and hence only the minimum number of new elements are formed. The decomposition algorithm and its associated degeneracies and treatment of the threshold at which the level set is close enough to the parent edge to “snap to the grid” are described in full detail in [24].

### 3.3 Level set equations

An interface capturing method, specifically a level set method, is used to represent the interface. In this approach a scalar level set field is used to approximate the signed distance to the interfaces. A signed distance function is an implicit function defined in  $N$ -space (in our case a 2 or 3D domain) such that its magnitude is equal to the distance from the interface in  $N - 1$  space (a line or surface) [28]. The sign of this signed distance function determines whether a point is interior or exterior to the level set surface. We will assume that interfaces move with the surrounding fluid, and therefore the level set distance function evolves with a simple advection equation,

$$\frac{\partial \psi}{\partial t} + \mathbf{u} \cdot \nabla \psi = 0. \quad (3.3.1)$$

The zero level set of the level set field,  $\psi$ , represents the location of the interface.

Although the level set field gets initialized as a signed distance function, depending on the fluid flow characteristics,  $\psi$  will eventually get distorted away from a true signed distance function. This equation correctly evolves the zero level set, but does not preserve the signed-distance property. Consequently, the level set field must be periodically reinitialized. In this work, this is accomplished by recomputing the distance to the reconstructed piecewise linear interface. In practice, we see degradation of the solution when reinitialization is performed too frequently. This is possibly due to the fact that the zero level set gets reinitialized as a piecewise linear function instead of remaining a smooth, higher order function.



# Chapter 4

## Results

In this chapter we compare CDFEM to ALE methods and traditional diffuse level set methods, perform V&V for the code implementation for electrohydrodynamic flows and demonstrate the code capabilities for more realistic problems in 3D.

### 4.1 Interfacial method comparison

We present a simulation comparison between an Arbitrary Lagrangian-Eulerian (ALE) method, a diffuse level set method and CDFEM in Figure 4.1. We choose to model a droplet falling due to gravity, which impacts the surface of an identical liquid below it and eventually merges with the fluid below. Note that this is a difficult problem to solve because it is hard to resolve the lubrication layer that develops between the droplet and the impact surface without special treatment of the lubrication layer. Note that no such special treatment is performed here. All of the simulations presented in Figure 4.1 are computed in Aria. As we demonstrate here, the ALE method will produce poor quality elements as the mesh deforms in time. Even with edge swapping algorithms and dynamic mesh refinement on large elements (simulations not shown), element inversion will occur prior to any topological change. For such a method to capture the merging process, it would require adaptively inserting and deleting elements. In this case, element deletion is the largest obstacle, as dynamic mesh refinement and edge flipping can greatly aid in correcting for the large, stretched elements that form at the top of the drop as it begins to fall. The thin region of oil between the water droplet and the water reservoir prior to impact is where elements require removal in order for merging to take place.

Both the diffuse level set method and CDFEM are able to handle the topological change of droplet merging. However, both methods will tend to over predict coalescence due to the nature of the level set algorithm, which is only as sensitive as the mesh width provided that the width of the lubrication layer is wider than one mesh width, these methods can resolve it, but beyond that the droplet are assumed to be in contact and merge. For a diffuse level set method the effective mesh width is that of the parent geometry, and for CDFEM (a sharp interface method) the mesh width prior to merging can be considerably smaller due to mesh cutting along the interface as it evolves closer to the impact surface. For this reason, CDFEM has the potential to perform better than a traditional level set method, provided

that the upper and lower interfaces are not attempting the cut the same element. The diffuse level set method requires mesh refinement in order to resolve the lubrication layer. CDFEM handles this test problem better than a diffuse level set method without adaptation since it is able to track the interface along element edges. In addition, The Krino library can handle CDFEM adaptive mesh refinement near the interface, and this tool can greatly aid in accurately predicting coalescence.

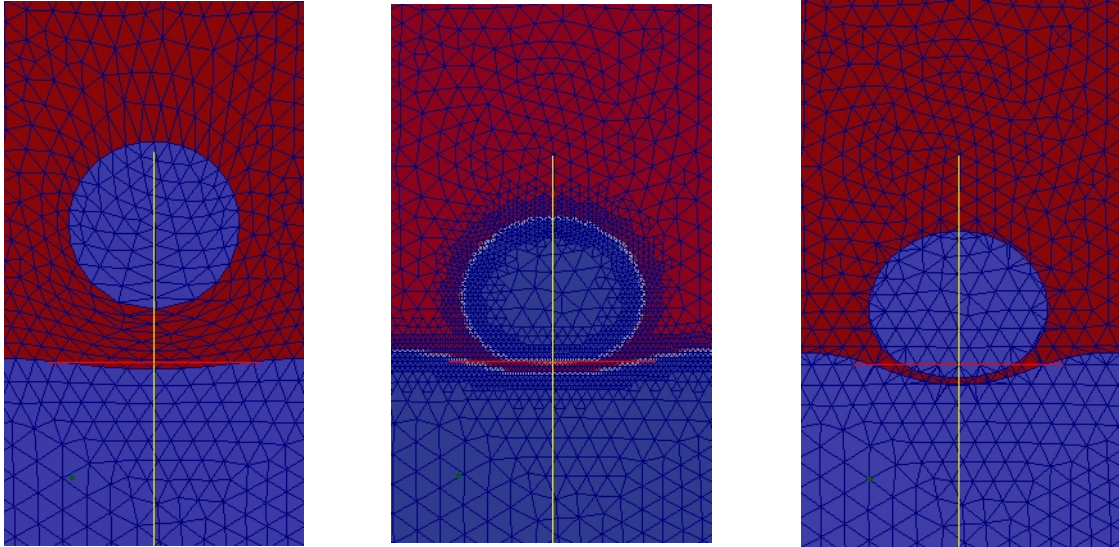


**Figure 4.1.** Simulations of a droplet falling due to gravity. Left Panel: ALE method, Center Panel: Diffuse level set method, Right Panel: CDFEM.

## 4.2 Verification

Code verification is of vital importance to ensure proper implementation and verify convergence rates. The code changes to the SIERRA/Aria framework that have been made in order to simulate the dynamics of charged droplets include adding the Maxwell stress tensor to the Navier-Stokes momentum equation, a charge density equation in both the bulk and on the surface, as well as new boundary conditions for the voltage equation and charge density equation.

### 4.2.1 Maxwell stress tensor verification: viscous flow due to charge

We choose an analytic solution to the voltage and momentum equations on a  $[0, 1] \times [0, 1]$  domain and use the corresponding boundary conditions to solve our system of equations for the fluid velocity given the presence of an electric force due to the Maxwell stress tensor.

For simplicity, we choose a constant bulk charge,  $\rho_V = 0.2$ , a constant permittivity,  $\varepsilon = 0.1$ , a constant viscosity,  $\mu = 0.1$ , as well as neglecting inertial forces and pressure. This set of assumptions provides us with a straightforward check for the Maxwell stress tensor implementation, since we avoid solving the continuity equation and the charge density equation. Our system of equations is

$$\nabla \cdot (\varepsilon \nabla \phi(x, y)) = -\rho_V \quad (4.2.1)$$

$$2\mu \nabla^2 \mathbf{u}(x, y) = -\rho_V \nabla \phi(\mathbf{x}, \mathbf{y}) \quad (4.2.2)$$

We require a velocity solution that varies in both  $x$  and  $y$ . The corresponding analytic solution of these equations is chosen as

$$\phi(x, y) = \frac{1}{2}(x^2 + y^2) \quad (4.2.3)$$

$$u(x, y) = -\frac{1}{2}xy^2 \quad (4.2.4)$$

$$v(x, y) = \frac{1}{2}x^2y \quad (4.2.5)$$

and thus  $E_x = -x$  and  $E_y = -y$ . The analytic solution is used to apply boundary conditions for both voltage and velocities at  $x = 0, 1$  and  $y = 0, 1$ . We simulate this steady-state problem in Aria and perform a mesh refinement study, which demonstrates that our implementation is correct and is second order accurate for velocity (see Figure 4.2).

## 4.2.2 Charge density verification: Relaxation on a spherical drop

Consider a charged drop of radius  $R_0$  in an isotropic fluid (see Figure 4.3), insulated from external electric forces by a spherical insulator of radius  $R_1$  concentric with the drop. Because of symmetry and incompressibility, the fluid remains at rest, even though the charge will not. Assuming magnetic effects can be neglected, the electric field can be written as the gradient of voltage,  $\varphi$ ,

$$\nabla \cdot (\varepsilon \nabla \phi) = -\nabla \cdot (\varepsilon \mathbf{E}) = -\rho_V \quad (4.2.6)$$

### Bulk charge

We assume the charge outside the drop is negligible, that ion mobility is negligible and we can make Ohm's law assumption, and conductivity and permittivity are uniform and constant. Then interior to the drop the charge moves according to the equation

$$\frac{\partial \rho_V}{\partial t} = -\nabla \cdot \sigma \mathbf{E} = \sigma \nabla \cdot \mathbf{E} = -\frac{\sigma}{\varepsilon} \rho_V. \quad (4.2.7)$$

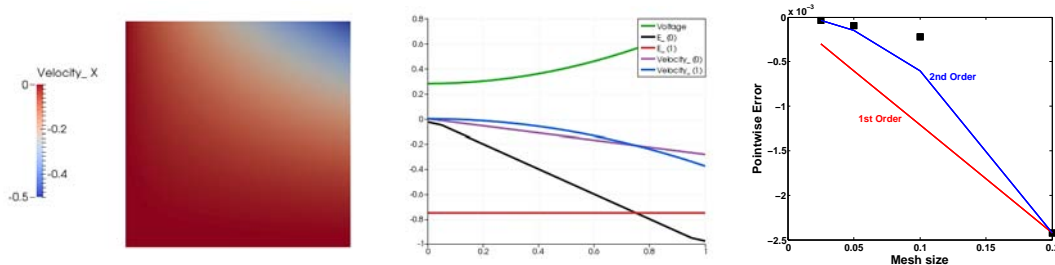


**Figure 4.2.** Verification study for Maxwell stress tensor: (Left) Velocity profile on  $[0, 1] \times [0, 1]$  domain for  $u(x, y) = 0.5xy^2$ . (Center) Slice through domain for all variable at  $x = 0.75$ . (Right) Demonstrating second order accuracy of velocity profile with applied electrical force. Four meshes are analyzed (represented by solid squares).

We apply an initial condition for charge on the drop to be  $\rho_V^0(R)$  to be only a function of  $R$  (or constant). With this initial condition, equation 4.2.7 can be easily solved, obtaining

$$\rho^e(R, t) = \rho_V^0(R)e^{-\sigma t/\varepsilon}. \quad (4.2.8)$$

## Surface charge

Next we compute the surface charge,  $q(t)$ , as a function of time given some uniform initial charge  $q_0$ . The governing equation for the surface charge is obtained from conservation of total charge,  $Q$  (i.e. charge that decays in the bulk remains at the surface of the drop)

$$4\pi R_0^2 q_0 + 4\pi \int_0^{R_0} \rho_V^0(R) R^2 dR = Q = 4\pi R_0^2 q(t) + 4\pi \int_0^{R_0} \rho_V(R, t) R^2 dR. \quad (4.2.9)$$

The expression on the left represents the total charge at time  $t = 0$ , while the expression on the right represents the total charge at time  $t \geq 0$ . The two integral expressions represent the total bulk charge in the interior of the drop. We apply equation 4.2.8 for the bulk charge and solve for the surface charge

$$q(t) = q_0 + q_d(1 - e^{-\sigma t/\varepsilon}) \quad (4.2.10)$$

where we have defined

$$q_d = \frac{1}{R_0^2} \int_0^{R_0} \rho_V^0(R) R^2 dR. \quad (4.2.11)$$

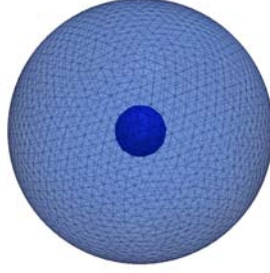


**Figure 4.3.** Geometry for verification problem: two concentric spheres. The interior sphere is conductive and carries a charge. The outer sphere is an insulator.

Here,  $q_0$  represents the initial bulk charge per unit surface area, and  $q_d$  is the total amount of surface charge that can be obtained from the bulk.

### Voltage

By symmetry, voltage is a function only of time and the distance,  $R$ , to the center of the drop:  $\varphi = \varphi(R, t)$ . Thus, written in spherical coordinates equation 4.2.6 becomes

$$\frac{1}{R^2} \frac{\partial}{\partial R} \left( R^2 \frac{\partial \varphi}{\partial R} \right) = -\frac{\rho_V}{\varepsilon} = -\frac{1}{\varepsilon} \rho_V^0(R) e^{-\sigma t/\varepsilon}. \quad (4.2.12)$$

We can decompose the potential homogeneous and particular solutions,

$$\varphi = \varphi_h + \varphi_p,$$

where the homogeneous solution,  $\varphi_h$ , satisfies the Laplace equation with nonzero boundary conditions and the particular solution,  $\varphi_p$ , is due only to the bulk charge, and is zero outside the interior sphere.

The voltage,  $\varphi_p$ , due to the bulk charge in the drop can be found by integrating equation 4.2.12 directly and imposing zero boundary conditions everywhere.

$$\varphi_p(R, t) = \varphi_0(R) e^{-\sigma t/\varepsilon_d} \quad \text{for } R < R_0 \quad (4.2.13)$$

where

$$\varphi_0(R) = \frac{1}{\varepsilon_d} \int_R^{R_0} \frac{1}{\zeta^2} \int_0^\zeta \xi^2 \rho_0^e(\xi) d\xi d\zeta \quad (4.2.14)$$

The electric field due to the bulk charge can be computed by differentiating:

$$E_p(R, t) = -\frac{\partial \varphi_p}{\partial R} = \frac{e^{-\sigma t/\varepsilon_d}}{\varepsilon_d R^2} \int_0^R \xi^2 \rho_0^e(\xi) d\xi \quad \text{for } R < R_0 \quad (4.2.15)$$

For example, when the charge distribution is initially uniform,

$$\varepsilon_d \varphi_p(R) = \frac{1}{6}(R_0^2 - R^2)\rho_0^e e^{-\sigma t/\varepsilon_d} \quad \text{and} \quad \varepsilon_d E_p = \frac{R}{3}\rho_0^e e^{-\sigma t/\varepsilon_d} \quad \text{for} \quad R < R_0$$

Comparing Equations 4.2.11 and 4.2.15, we see that the electric field at the boundary is given by

$$\varepsilon_d E(R_0^-) = - \lim_{R \rightarrow R_0^-} \varepsilon \frac{\partial \varphi_p}{\partial R} = q_d e^{-\sigma t/\varepsilon_d} = \varepsilon_x E_p(R_0^+) \quad (4.2.16)$$

where the last equality follows from the boundary condition on the electric field when  $q(t) = 0$ , and  $\varepsilon_x$  is the permittivity on the exterior of the drop.

The homogeneous solution,  $\varphi_h$ , satisfies a radial Laplace equation which can be directly integrated to obtain

$$\varphi_h(R) = \begin{cases} a_1 + a_2/R & R < R_0 \\ b_1 + b_2/R & R > R_0 \end{cases}$$

With the condition of finite voltage at the center, get  $a_2 = 0$ . Grounding the voltage at the outside boundary, get  $b_2 = -R_1 b_1$ . Imposing continuity on the surface of the drop, we get  $a_1 = b_1 + b_2/R_0 = b_1(1 - R_1/R_0)$ . Now, supply the jump condition for the electric field based on the charge density,  $q$ , on the surface of the drop:  $\|\varepsilon \mathbf{E}\| \cdot \mathbf{n} = q$ . Because  $\varphi_h$  is constant inside the drop, there is no contribution to the electric field from the surface charge. Hence, the field on the interior boundary of the drop is due only to the bulk charge, and is given by equation 4.2.16. By symmetry there is no tangential component to the electric field, so the jump condition on the electric field can be reduced to the following:

$$\begin{aligned} \lim_{R \rightarrow R_0^+} \varepsilon_x E_x(R, t) &= q(t) + \lim_{R \rightarrow R_0^-} \varepsilon_d E_d(R, t) \\ &= q(t) + q_d e^{-\sigma t/\varepsilon_d} \\ &= q_0 + q_d \end{aligned}$$

This can be evaluated by differentiating the exterior voltage:

$$\lim_{R \rightarrow R_0^+} \frac{\partial \varphi_h}{\partial R} = b_1 \lim_{R \rightarrow R_0^+} \frac{\partial}{\partial R} \left( 1 - \frac{R_1}{R} \right) = \frac{R_1 b_1}{R_0^2} = -\frac{1}{\varepsilon_x} (q_0 + q_d)$$

Putting everything together, the total voltage is

$$\begin{aligned} \varphi(R, t) &= \varphi_0(R) e^{-\sigma t/\varepsilon} + \frac{R_0^2}{\varepsilon_x} \left( \frac{1}{R_0} - \frac{1}{R_1} \right) (q_0 + q_d) \quad \text{when} \quad R < R_0 \\ \varphi(R, t) &= \frac{R_0^2}{\varepsilon_x} \left( \frac{1}{R} - \frac{1}{R_1} \right) (q_0 + q_d) \quad \text{when} \quad R > R_0 \end{aligned} \quad (4.2.17)$$

From equation 4.2.17, we see regardless of initial conditions, the exterior voltage and electric field are independent of the behavior of the bulk charge, but rather, depend only on the total charge in the drop.

## Uniform initial charge

Assuming  $\rho_0^e(R) = \rho_0^e$  is uniform and the initial charge is zero,  $q_0 = 0$ , we obtain the following simplified analytic solution:

1. Bulk Charge:

$$\rho^e(R, t) = \rho_0^e e^{-\sigma t/\varepsilon_d} \quad \text{for } R < R_0$$

2. Surface Charge:

$$q(t) = \frac{1}{3} R_0 \rho_0^e (1 - e^{-\sigma t/\varepsilon_d})$$

3. Voltage:

$$\begin{aligned} \text{for } R < R_0 \quad \varphi(R, t) &= \frac{\rho_0^e}{6\varepsilon_d} (R_0^2 - R^2) e^{-\sigma t/\varepsilon} + \frac{R_0^3 \rho_0^e}{3\varepsilon_x} \left( \frac{1}{R_0} - \frac{1}{R_1} \right) \\ \text{for } R \geq R_0 \quad \varphi(R, t) &= \frac{R_0^3 \rho_0^e}{3\varepsilon_x} \left( \frac{1}{R} - \frac{1}{R_1} \right) \end{aligned}$$

We set up this test problem in Aria with the following parameters:

$\rho_V^0$	=	$1.0 \times 10^{-9}$	g mm <sup>3</sup>
$\varepsilon$	=	$7.1 \times 10^{-10}$	sec-S/m
$\sigma$	=	$4.0 \times 10^{-4}$	S/m
$t_f$	=	$1.0 \times 10^{-6}$	sec
$R_0$	=	1.0	mm
$R_1$	=	1.5	mm

and thus from equation 4.2.7 we have

$$\rho_V(t_f) = \rho_V^0 \exp(-\sigma t_f/\varepsilon) = 5.693 \times 10^{-10}. \quad (4.2.18)$$

We show our results from this simulation in Figure 4.4. The charge decays exponentially within the sphere and charge remains at the surface - although it does not build up as if total charge were preserved. There are two reasons for this behavior. One, we do not account for charge accumulation at the surface since charge is only computed in the bulk here, and two, there is error associated with our no-flux boundary conditions. However, it should be noted that the voltage is quite similar to the analytic solution (assuming that charge is allowed to accumulate at the interface), and therefore this suggests that the surrounding fluid dynamics are not extremely sensitive to charge conservation in this parameter regime (at least this is true for droplet deformation - coalescence may be very dependent).

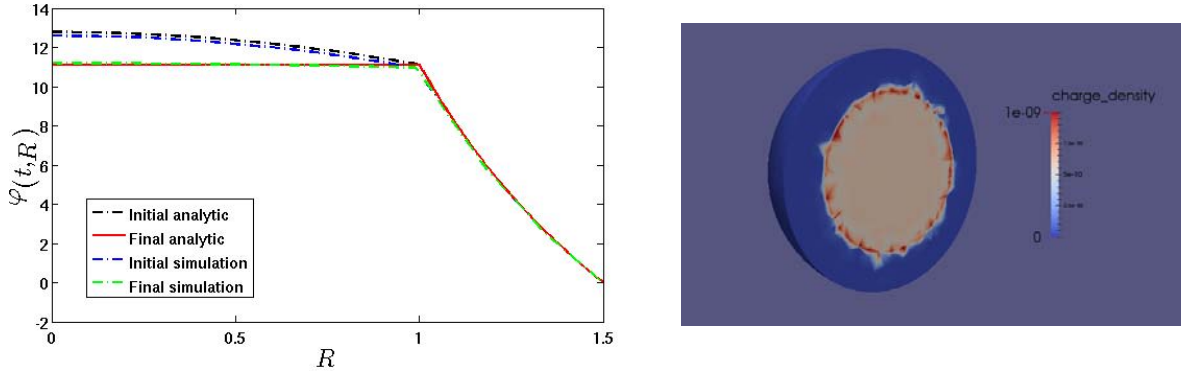


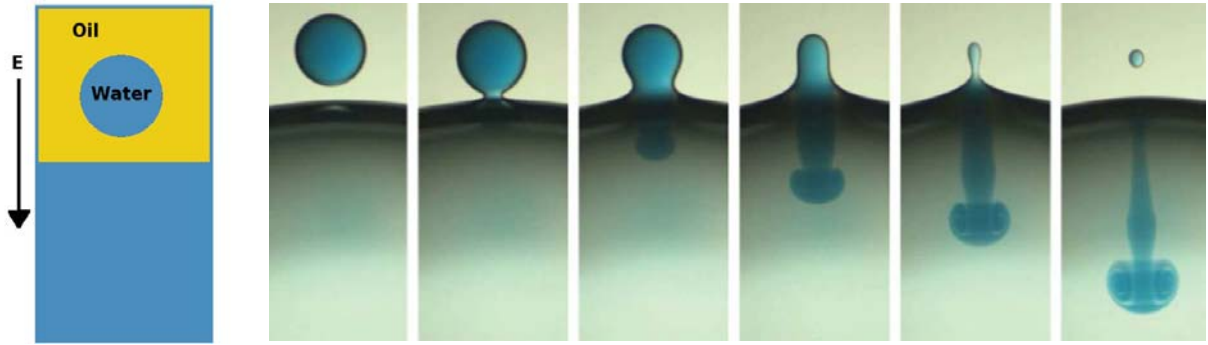
**Figure 4.4.** Verification for charge density implementation: Left: Voltage potential comparison between analytic solution and computational solution. Right: Charge density decays appropriately, however for simple no-flux boundary conditions, charge at the interface remains constant or builds up much slower than it should if total charge were preserved.

### 4.3 Validation

Hamlin *et al.* [16] conducted a series of experiments of electrically driven coalescence (see Figure 4.5). An electric field is applied by forcing a potential difference across the domain. The water droplet is a salt solution of KCl that gains charge initially from the top electrode via dielectrophoresis. Once the droplet is charged, it moves toward the lower water surface and coalesces, forming a daughter droplet after pinch-off. In this paper it is discovered that the convective time scale is important to the charge transfer dynamics.

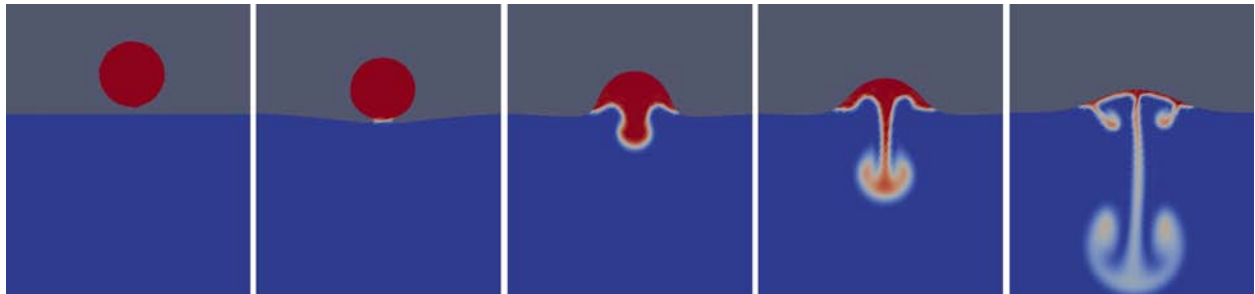
The simulation results we compare these experiments to should not be exact since the computations are in two-dimensions and hence surface tension effects will vary. The oil to water viscosity ratio for the experiment was approximately 350 and the ratio for the computation is 500. Due to the viscosity ratio, the time step for the water droplet as it approaches the contact surface is fairly slow. The surface tension is assumed to be 40 g-sec<sup>-2</sup>, which drives coalescence after the aqueous bridge forms. However, once contact occurs, the time step is driven down quickly by a factor of 25 in order to capture coalescence and keep the simulation stable. Dye injection for the simulation is accomplished by including a benign initial species concentration in the droplet with a low diffusivity to keep track of how the fluid originating in the droplet distributes into the lower fluid upon contact.

We see in Figure 4.6 that our computational results match well qualitatively with Hamlin *et al.*'s experimental work, although we are not able to distinguish the formation of a daughter droplet for this case. Since the simulation is in two dimensions only the surface tension effects and pressure drop are different. In addition, the time scale for the charge density was chosen to be much slower than is physically reasonable, since the fluid time scale and the charge



**Figure 4.5.** Electrically driven partial coalescence, showing vortex penetration. The surrounding oil is highly viscous. The water droplet contains blue food dye for visualization of the penetrating vortex, which demonstrates that the fluid advection time scale should not be neglected. Figure courtesy of William Ristenpart [16].

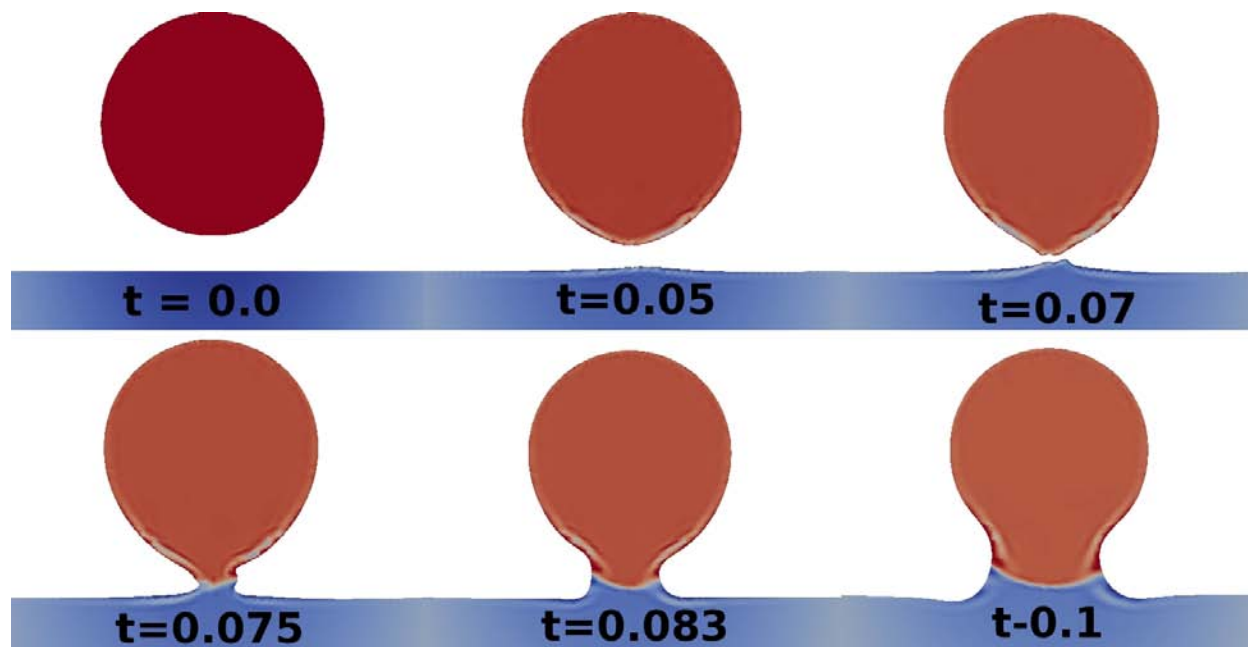
density time scales are very different. Charge density should equilibrate much more quickly in reality than it does in this simulation and it is also predicted that the daughter droplet has a opposite charge from the parent drop since opposite charge ought to accumulate at the surface of the drop, and may be the reason for the daughter droplet to pinch-off. This computational experiment should be revisited once surface charge can be correctly accounted for using shell elements and the full surface charge density equation.



**Figure 4.6.** Simulation result for validation experiment to be compared with merging droplet and vortex formation in [16] and shown in Figure 4.5.

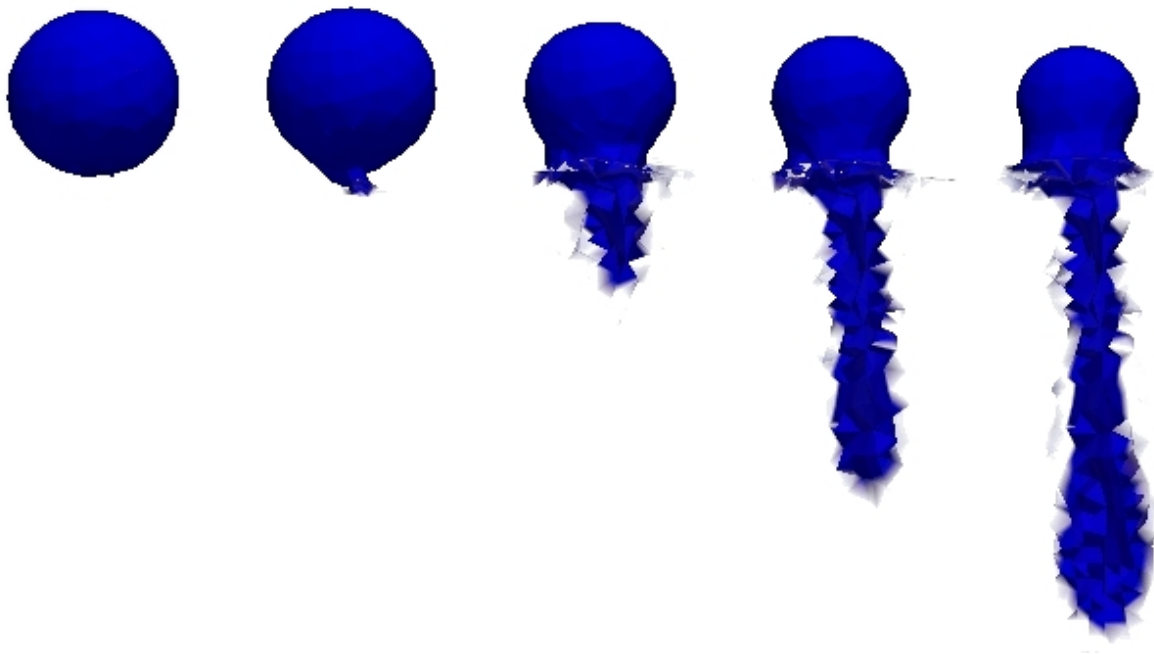
## 4.4 Droplet coalescence and cone formation

Figure 4.7 shows the formation of a Taylor cone at the bottom end of a charged droplet due to an applied electric field. As opposed to a droplet driven downward by gravity, a charged droplet moves with a pointed tip that sharpens with charge and the strength of the electric field. Upon contact with the impact surface, the aqueous bridge is asymmetric. This asymmetry is due to the fact that the neck region is so thin that the mesh becomes visible; the neck region is only about 5-10 elements wide. As coalescence begins to take place, this asymmetry disappears, but resolving the aqueous bridge at contact is very important to the resulting dynamics of the system. In these computational experiments, viscosity is uniform in the water and oil and surface tension lower than in the penetrating vortex case described above.



**Figure 4.7.** Simulation results for cone formation of a charged drop as it impacts an oppositely charged water surface. The aqueous bridge that forms is asymmetric, resulting from the mesh visibility at the neck width (about 5-10 elements wide).

In order to demonstrate the code capability in three dimensions, we perform simulations shown in Figure 4.8. It is clear that a refined mesh is required in order to accurately capture the neck region without mesh artifacts.



**Figure 4.8.** 3D charged droplet simulation. Blue color represents “dye injection” from droplet fluid into the lower water reservoir.



# Chapter 5

## Conclusion

Accurate and stable interface-tracking methods capable of capturing and predicting coalescence and break-up of interfaces are currently a major challenge in the computational science community. Including electric forces and charge pose further challenges due to the complexity of electrostatic and hydrodynamic interactions involved in coalescence. Therefore, we require a novel modeling approach to understand this phenomenon. This report describes a CDFEM approach to solving low to intermediate Reynolds number electrohydrodynamic flow problems that has the potential to be adapted for use in a variety of application areas including lab on a chip technology, purifying biodiesel fuel, and electrowetting. This capability is available within Sandia's internal Sierra codes. CDFEM treats interfacial dynamics by cutting elements along the boundary such that the interface is exactly aligned with element surfaces. This approach has many advantages including straightforward implementation of interfacial Dirichlet boundary conditions, zero interfacial thickness, the ability to handle complex topologies using unstructured meshes, and good convergence for stationary problems. We are able to demonstrate the method's validity with analytic verification problems and validation problems that we can compare to experimental data. This investigation is able to demonstrate droplet electrocoalescence, however the bouncing phenomenon was not able to be simulated for two reasons: (1) the time scale for which charge density decays was considerably slowed down in this simulations in order to get a large enough time step to allow for computation. Experiments suggest that the charge density redistributes almost instantaneously and this is what causes the aqueous bridge to pinch off (since there is no longer a force pushing the droplets together). (2) This phenomenon should only be seen in three dimensions, which is computationally demanding on an adequately refined mesh. The first reason could be experimented with by restarting a simulation without any non-uniform charge density distribution once the aqueous bridge has formed. It is predicted that in this case, the bridge would pinch off due to pressure and surface tension minimization forces. The second obstacle could soon be overcome with the axisymmetric capability for CDFEM simulations in Aria. This capability would allow for effectively three-dimensional rotationally symmetric simulations to be simulated with the computational cost of a two-dimensional simulation.



# References

- [1] L. L. Agostinho, E. C. Fuchs, S. J. Metz, C. U. Yurteri, and J. C. M. Marijinissen. Reverse movement and coalescence of water microdroplets in electrohydrodynamic atomization. *Physical Review E*, 84:026317 1–12, 2011.
- [2] James C Bird, William D Ristenpart, Andrew Belmonte, and Howard A Stone. Critical angle for electrically driven coalescence of two conical droplets. *Physical review letters*, 103(16):164502, 2009.
- [3] Erik Bjørklund. The level-set method applied to droplet dynamics in the presence of an electric field. *Computers & Fluids*, 38(2):358–369, 2009.
- [4] R Bruinsma, M Goulian, and P Pincus. Self-assembly of membrane junctions. *Biophysical journal*, 67(2):746–750, 1994.
- [5] Paul Calvert. Inkjet printing for materials and devices. *Chemistry of Materials*, 13(10):3299–3305, 2001.
- [6] Vittorio Cristini, Jerzy Bławdziewicz, and Michael Loewenberg. An adaptive mesh algorithm for evolving surfaces: simulations of drop breakup and coalescence. *Journal of Computational Physics*, 168(2):445–463, 2001.
- [7] Marcela A Cruchaga, Diego J Celentano, and Tayfun E Tezduyar. A numerical model based on the mixed interface-tracking/interface-capturing technique (mitict) for flows with fluid–solid and fluid–fluid interfaces. *International journal for numerical methods in fluids*, 54(6-8):1021–1030, 2007.
- [8] Meizhong Dai and David P Schmidt. Adaptive tetrahedral meshing in free-surface flow. *Journal of Computational Physics*, 208(1):228–252, 2005.
- [9] Jean Donea, Antonio Huerta, J-Ph Ponthot, and Antonio Rodríguez-Ferran. Arbitrary lagrangian–eulerian methods. *Encyclopedia of computational mechanics*, 2004.
- [10] Aaron M Drews, Hee-Young Lee, and Kyle Bishop. Ratcheted electrophoresis for rapid particle transport. *Lab on a Chip*, 2013.
- [11] John S Eow, Mojtaba Ghadiri, Adel O Sharif, and Trevor J Williams. Electrostatic enhancement of coalescence of water droplets in oil: a review of the current understanding. *Chemical engineering journal*, 84(3):173–192, 2001.
- [12] Ali Fallah-Araghi, Jean-Christophe Baret, Michael Ryckelynck, and Andrew D Griffiths. A completely in vitro ultrahigh-throughput droplet-based microfluidic screening system for protein engineering and directed evolution. *Lab on a Chip*, 12(5):882–891, 2012.

- [13] Juan Fernández de La Mora. The fluid dynamics of taylor cones. *Annu. Rev. Fluid Mech.*, 39:217–243, 2007.
- [14] Shuai Gong, Ping Cheng, and Xiaojun Quan. Lattice boltzmann simulation of droplet formation in microchannels under an electric field. *International Journal of Heat and Mass Transfer*, 53(25):5863–5870, 2010.
- [15] D. G. Griffiths. *Introduction to Electrodynamics*. Prentice-Hall Inc., 1989.
- [16] BS Hamlin, JC Creasey, and WD Ristenpart. Electrically tunable partial coalescence of oppositely charged drops. *Physical Review Letters*, 109(9):094501, 2012.
- [17] Sebastian Helmsdorfer and Peter Topping. Bouncing of charged droplets: An explanation using mean curvature flow. *arXiv preprint arXiv:1302.4862*, 2013.
- [18] Jinsong Hua, Liang Kuang Lim, and Chi-Hwa Wang. Numerical simulation of deformation/motion of a drop suspended in viscous liquids under influence of steady electric fields. *Physics of Fluids*, 20:113302, 2008.
- [19] Joseph B Keller, Paul A Milewski, and Jean-Marc Vanden-Broeck. Merging and wetting driven by surface tension. *European Journal of Mechanics-B/Fluids*, 19(4):491–502, 2000.
- [20] Lou Kondic. Instabilities in gravity driven flow of thin fluid films. *Siam review*, 45(1):95–115, 2003.
- [21] Zhaorui Li, Farhad A Jaber, and Tom I-P Shih. A hybrid lagrangian–eulerian particle-level set method for numerical simulations of two-fluid turbulent flows. *International journal for numerical methods in fluids*, 56(12):2271–2300, 2008.
- [22] Darren R Link, Erwan Grasland-Mongrain, Agnes Duri, Flavie Sarrazin, Zhengdong Cheng, Galder Cristobal, Manuel Marquez, and David A Weitz. Electric control of droplets in microfluidic devices. *Angewandte Chemie International Edition*, 45(16):2556–2560, 2006.
- [23] J. M. Lopez-Herrera, S. Popinet, and M. A. Herrada. A charge-conservative approach for simulating electrohydrodynamic two-phase flows using volume-of-fluid. *Journal of Computational Physics*, 230:1939–1955, 2011.
- [24] D R. Noble, E. P. Newren, and J. B. Lechman. A conformal decomposition finite element method for modeling stationary fluid interface problems. *International Journal for Numerical Methods in Fluids*, 63:725–742, 2010.
- [25] Ricardo H Nochetto and Shawn W Walker. A hybrid variational front tracking-level set mesh generator for problems exhibiting large deformations and topological changes. *Journal of Computational Physics*, 229(18):6243–6269, 2010.
- [26] Patrick K Notz, Samuel R Subia, Matthew M Hopkins, Harry K Moffat, and David R Noble. Aria 1.5 user manual. *Sandia Report*, 2734:2007, 2007.

- [27] Harry T Ochs and Robert R Czys. Charge effects on the coalescence of water drops in free fall. *Nature*, 327:606–608, 1987.
- [28] Stanley Osher and Ronald Fedkiw. *Level set methods and dynamic implicit surfaces*, volume 153. Springer, 2003.
- [29] Yu Pan and Kazuhiko Suga. Numerical simulation of binary liquid droplet collision. *Physics of Fluids*, 17:082105, 2005.
- [30] B. P. Van Poppel, O. Desjardins, and J. W. Daily. A ghost fluid, level set methodology for simulating multiphase electrohydrodynamic flows with application to liquid fuel injection. *Journal of Computational Physics*, 229:7977–7996, 2010.
- [31] Shaoping Quan, Jing Lou, and David P Schmidt. Modeling merging and breakup in the moving mesh interface tracking method for multiphase flow simulations. *Journal of Computational Physics*, 228(7):2660–2675, 2009.
- [32] Shaoping Quan and David P Schmidt. A moving mesh interface tracking method for 3d incompressible two-phase flows. *Journal of Computational Physics*, 221(2):761–780, 2007.
- [33] Jonathan Raisin, Jean-Luc Reboud, and Pierre Atten. Electrically induced deformations of water–air and water–oil interfaces in relation with electrocoalescence. *Journal of Electrostatics*, 69(4):275–283, 2011.
- [34] W. D. Ristenpart, J. C. Bird, A. Belmonte, F. Dollar, and H. A. Stone. Non-coalescence of oppositely charged drops. *Nature*, 461:377–380, 2009.
- [35] Scott A Roberts, David R Noble, Eric M Benner, and P Randall Schunk. Multiphase hydrodynamic lubrication flow using a three-dimensional shell finite element model. *Computers & Fluids*, 2012.
- [36] D. A. Saville. Electrohydrodynamics: The taylor-melcher leaky dielectric model. *Annu. Rev. Fluid Mech.*, 29:27–64, 1997.
- [37] G. Tomar, D. Gerlach, G. Biswas, N. Alleborn, A. Sharma, F. Durst, S. W. J. Welch, and A. Delgado. Two-phase electrohydrodynamic simulations using a volume-of-fluid approach. *Journal of Computational Physics*, 227:1267–1285, 2007.
- [38] Shawn W Walker and Benjamin Shapiro. Modeling the fluid dynamics of electrowetting on dielectric (ewod). *Microelectromechanical Systems, Journal of*, 15(4):986–1000, 2006.
- [39] Maria Yokota and Ko Okumura. Dimensional crossover in the coalescence dynamics of viscous drops confined in between two plates. *Proceedings of the National Academy of Sciences*, 108(16):6395–6398, 2011.
- [40] Michele Zagnoni, Guillaume Le Lain, and Jonathan M Cooper. Electrocoalescence mechanisms of microdroplets using localized electric fields in microfluidic channels. *Langmuir*, 26(18):14443–14449, 2010.

- [41] Junfeng Zhang and Daniel Y Kwok. A 2d lattice boltzmann study on electrohydrodynamic drop deformation with the leaky dielectric theory. *Journal of Computational Physics*, 206(1):150–161, 2005.

## A The axisymmetric Maxwell stress tensor

In an axisymmetric setup, the electric field can be written as  $\mathbf{E} = E_r \mathbf{e}_r + E_z \mathbf{e}_z$ . Most significantly, the aximuthal coordinate is zero:  $E_\theta = 0$ . Then the Maxwell Stress Tensor can be written as follows:

$$\begin{aligned} \mathbf{T}^e &= \varepsilon \varepsilon_0 \begin{pmatrix} E_r E_r & 0 & E_r E_z \\ 0 & 0 & 0 \\ E_z E_r & 0 & E_z E_z \end{pmatrix} - \frac{1}{2} \alpha \varepsilon \varepsilon_0 \begin{pmatrix} E^2 & 0 & 0 \\ 0 & E^2 & 0 \\ 0 & 0 & E^2 \end{pmatrix} \\ &= \frac{1}{2} \varepsilon \varepsilon_0 \begin{pmatrix} 2E_r^2 - \alpha E^2 & 0 & 2E_r E_z \\ 0 & -\alpha E^2 & 0 \\ 2E_z E_r & 0 & 2E_z E_z - \alpha E^2 \end{pmatrix} \end{aligned}$$

In cylindrical coordinates, the divergence of a rank 2 tensor is given by

$$\nabla \cdot \begin{pmatrix} S_{rr} & S_{r\theta} & S_{rz} \\ S_{\theta r} & S_{\theta\theta} & S_{\theta z} \\ S_{zr} & S_{z\theta} & S_{zz} \end{pmatrix} = \begin{pmatrix} \frac{\partial S_{rr}}{\partial r} + \frac{S_{rr}}{r} + \frac{1}{r} \frac{\partial S_{\theta r}}{\partial \theta} + \frac{\partial S_{zr}}{\partial z} - \frac{S_{\theta\theta}}{r} \\ \frac{1}{r} \frac{\partial S_{\theta\theta}}{\partial \theta} + \frac{\partial S_{r\theta}}{\partial r} + \frac{S_{r\theta}}{r} + \frac{S_{\theta r}}{r} + \frac{\partial S_{z\theta}}{\partial z} \\ \frac{\partial S_{zz}}{\partial z} + \frac{\partial S_{rz}}{\partial r} + \frac{S_{rz}}{r} + \frac{1}{r} \frac{\partial S_{\theta z}}{\partial \theta} \end{pmatrix}$$

For a symmetric tensor in cylindrical coordinates, this expression simplifies:

$$\nabla \cdot \begin{pmatrix} S_{rr} & S_{r\theta} & S_{rz} \\ S_{\theta r} & S_{\theta\theta} & S_{\theta z} \\ S_{zr} & S_{z\theta} & S_{zz} \end{pmatrix} = \begin{pmatrix} \frac{\partial S_{rr}}{\partial r} + \frac{S_{rr}}{r} + \frac{\partial S_{zr}}{\partial z} - \frac{S_{\theta\theta}}{r} \\ 0 \\ \frac{\partial S_{zz}}{\partial z} + \frac{\partial S_{rz}}{\partial r} + \frac{S_{rz}}{r} \end{pmatrix} = \begin{pmatrix} \frac{1}{r} \frac{\partial}{\partial r} (r S_{rr}) + \frac{\partial S_{zr}}{\partial z} - \frac{S_{\theta\theta}}{r} \\ 0 \\ \frac{\partial S_{zz}}{\partial z} + \frac{1}{r} \frac{\partial}{\partial r} (r S_{rz}) \end{pmatrix}$$

Development of an axisymmetric capability in Aria is currently in progress for ALE methods, and having this capability in place for CDFEM is on the horizon. This form of the Maxwell stress tensor can be included in Aria for use in axisymmetric problems in the future. This will save dramatically on computational time compared to fully three-dimensional problems.

## B Summary of scales and constants

### B.1 Experimental timescales

1. Duration of Experiments:  $0.5\text{s} \leq \tau_{\text{exp}} \leq 0.8\text{s}$  [34].
2. Timescale for Aqueous Bridge:  $\tau_b \approx 8 \times 10^{-5}\text{s}$  [34].

### B.2 Length scales

1. Drop Radii:  $10^{-4}\text{m} \leq R_0 \leq 10^{-3}\text{m}$
2. Radius of bridge (meniscus):  $R_b \approx 10^{-5}\text{m}$
3. Drop Volume:  $2\mu\text{L} = 2 \times 10^{-9}\text{m}^3$

### B.3 Electromagnetic constants and scales

1. Applied Electric Field:  $10^5\text{V/m} \leq E_0 \leq 10^6\text{V/m}$
2. Permittivity of Free Space:  $\epsilon_0 \approx 8.854 \times 10^{-12}\text{F/m}$
3. Permeability of Free Space:  $\mu_0 = 4\pi \times 10^{-7}\text{V s/A m}$
4. Relative Permittivity of water:  $\epsilon_w \approx 80.1$  (wikipedia)
5. Relative Permeability of Water:  $\mu_w^M \approx 1.0$  (wikipedia)
6. Relative Permittivity of Polydimethylsiloxane:  $\epsilon_{\text{pms}} \ll \epsilon_w$
7. Electric Pressure:  $\epsilon_w \epsilon_0 E_0^2 \approx 63.74\text{Pa}$

### B.4 Fluid properties

1. Density of Water:  $\rho_w = 10^3\text{kg/m}^3$
2. Viscosity of Water:  $\mu_w = 10^{-3}\text{Pa s}$
3. Density of Polydimethylsiloxane:  $\rho_{\text{pms}} = 965.00\text{kg/m}^3$  [34].
4. Viscosity of Ca Polydimethylsiloxane:  $\mu_{\text{pms}} = 0.965\text{Pa s}$  (Google)
5. Water/Polydimethylsiloxane Surface Tension:  $\gamma_{wo} = 10^{-2}\text{N/m}$  [34].
6. Capillary Pressure:  $\gamma_{wo}/R_0 = 10\text{Pa}$

## B.5 Charged flow

1. Elementary Charge:  $e = 1.602176565(35) \times 10^{-19}\text{C}$
2.  $1\text{mol} = 6.02214078 \times 10^{23}$
3. Number of ions:  $0.2\text{mMKCl} = 0.2\text{mol}/\text{m}^3\text{KCl}$  [34].
4. Conductivity of deionized Water:  $4 \times 10^{-4}\text{S}/\text{m} \leq \sigma_w \leq 164 \times 10^{-4}\text{S}/\text{m}$  [34].
5. Conductivity of Polydimethylsiloxane:  $\sigma_{\text{pms}} \leq \sigma_w$  [34].
6. Ionic mobility of potassium:  $e\omega(\text{K}^+) \approx 7.15 \times 10^{-8}\text{m}^2/\text{V s}$
7. Ionic mobility of chloride:  $e\omega(\text{Cl}^-) \approx 6.85 \times 10^{-8}\text{m}^2/\text{V s}$
8. Diffusion coefficient of potassium:  $\omega(\text{K}^+)k_B \approx (2.65 \times 10^{-9}\text{m}^2/\text{s})/300\text{K}$
9. Diffusion coefficient of potassium:  $\omega(\text{Cl}^-)k_B \approx (1.70 \times 10^{-9}\text{m}^2/\text{s})/300\text{K}$
10. Charge Density:  $en_0 \approx 2 \times 10^4\text{C}/\text{m}^3$

## B.6 Thermodynamics

1. Room Temperature:  $T = 300\text{K}$
2. Boltzmann Constant:  $k_B = 1.3806488(13) \times 10^{-23}\text{J}/\text{K}$
3. Thermal Factor:  $k_B T = 4.14 \times 10^{-21}\text{J}$

## C Force comparisons

### C.1 Full process

We Use a lengthscale of  $R_0 = 1\text{mm}$  and a timescale of  $\tau = 0.1\text{s}$  [34]. Then the local forces at play scale as follows

1. Electric Force:  $f_e \sim \varepsilon^* E_0^2 / R_0 \approx (63.74\text{Pa}) / (10^{-3}\text{m}) \approx 6 \times 10^4\text{N}/\text{m}^3$
2. Viscous Force:  $f_\mu \sim \mu_u / R_0 \tau \approx (1\text{Pa s}) / (10^{-3}\text{m})(0.1\text{s}) \approx 10^4\text{N}/\text{m}^3$
3. Surface Force:  $f_c \sim \gamma / R_0^2 \approx (10^{-2}\text{N}/\text{m}) / (10^{-3}\text{m})^2 \approx 10^4\text{N}/\text{m}^3$
4. Inertia:  $f_i \sim \rho_l R_0 / \tau^2 \approx (10^3\text{kg}/\text{m}^3)(10^{-3}\text{m}) / (0.1\text{s})^2 \approx 100\text{N}/\text{m}^3$
5. Gravity:  $f_g \sim g(\rho_l - \rho_u) \approx (10\text{m}/\text{s}^2)(35\text{kg}/\text{m}^3) \approx 350\text{N}/\text{m}^3$

Clearly the electric force is dominant, while viscosity and surface forces are comparable, at about 1/6 the strength, inertia is about 1/100 the strength of these, and gravity is 3.5 times as strong as inertia

$$\frac{f_\mu}{f_e} \sim \frac{f_c}{f_e} \sim \frac{1}{6} \quad \frac{f_i}{f_e} \sim \frac{1}{6} \times 10^{-2} \quad \frac{f_g}{f_e} \sim \frac{1}{2} \times 10^{-2}$$

## C.2 Aqueous bridge

We Use a lengthscale of  $R_b = 10^{-5}\text{m}$  and a timescale of  $\tau_b = 10^{-5}\text{s}$  [34]. Then the local forces at play scale as follows

1. Electric Force:  $f_{e,b} \sim \varepsilon^* E_0 / R_b \approx (63.74\text{Pa}) / (10^{-5}\text{m}) \approx 6 \times 10^6 \text{N/m}^3$
2. Viscous Force:  $f_{\mu,b} \sim \mu_u / R_b \tau \approx (1\text{Pa s}) / (10^{-5}\text{m})(10^{-5}\text{s}) \approx 10^{10} \text{N/m}^3$
3. Surface Force:  $f_{c,b} \sim \gamma / R_b^2 \approx (10^{-2}\text{N/m}) / (10^{-5}\text{m})^2 \approx 10^8 \text{N/m}^3$
4. Inertia:  $f_{i,b} \sim \rho_l R_b / \tau_b^2 \approx (10^3 \text{kg/m}^3)(10^{-5}\text{m}) / (10^{-5}\text{s})^2 \approx 10^8 \text{N/m}^3$
5. Gravity:  $f_{g,b} \sim g(\rho_l - \rho_u) \approx (10\text{m/s}^2)(35\text{kg/m}^3) \approx 350 \text{N/m}^3$

Obtain the ratios:

$$\frac{f_{e,b}}{f_{\mu,b}} \sim 6 \times 10^{-4} \quad \frac{f_{c,b}}{f_{\mu,b}} \sim \frac{f_{i,b}}{f_{\mu,b}} \sim 10^{-2} \quad \frac{f_{g,b}}{f_{\mu,b}} \sim 3.5 \times 10^{-8}$$

Here, the viscous forces appear to dominate, while the surface tension and inertia come in second, at a relative strength of roughly  $10^{-2}$ . The electric force appears to have a relative strength of  $6 \times 10^{-4}$ , and the force of gravity appears to be completely negligible, having a relative strength of  $3.5 \times 10^{-8}$ . However, given that the scales for length and time are rough estimates, and the fact that we have not yet accounted for charge mobility within the drop, we should be cautious about neglecting any of these forces, except gravity.

## D Groupings

### D.0.1 Composite timescales

1. Magnetic Time:  $\tau_m = \mu\mu_0\sigma R_0^2 \leq 2 \times 10^{-14}\text{s}$
2. Charge Relaxation Time:  $\tau_e = \varepsilon\varepsilon_0/\sigma \approx 10^{-7}\text{s}$  [34].
3. Ion Drift Time:  $\tau_i = R_0/eE_0\omega_0 \approx 5 \times 10^{-2}\text{s}$
4. Viscous Capillary Time:  $\tau_{vc} = \mu R/\gamma \approx 10^{-1}\text{s}$  [34].

5. Electroviscous Time:  $\tau_{\text{ev}} = \mu_u / \varepsilon_w \varepsilon_0 E_0^2 \approx 1.5 \times 10^{-2} \text{s}$
6. Viscous Relaxation Time:  $\tau_\mu = \tau_{\text{ev}} \text{Md} = R_0^2 \rho_l / \mu_u \approx 10^{-3} \text{s}$
7. Inertial Capillary Time:  $\tau_{\text{Ca}} = \sqrt{\rho R^3 / \gamma}$

## D.1 Summary of dimensionless numbers

### D.1.1 Ratios of scales

1. Ratio of Characteristic Timescales

$$\eta = \frac{\tau_b}{\tau} \quad (\text{D.1})$$

2. Ratio of Characteristic Lengthscales

$$\zeta = \frac{R_b}{R_0} \quad (\text{D.2})$$

### D.1.2 Charge and ion conservation

1. Ion Peclet Number

$$\text{Pe}_i = \frac{R_0^2}{\omega_0 k_B T \tau} \approx 3.77 \times 10^3 \quad (\text{D.3})$$

2. Ion Drift Number

$$\text{Io} = \frac{k_B T}{e R_0 E_0} \approx 8.625 \times 10^{-5} \quad (\text{D.4})$$

3. Ion Charge Number

$$\text{Ch}_i = \frac{e n_0 R_0}{\varepsilon^* E_0} \approx 10^5 \quad (\text{D.5})$$

### D.1.3 Electrodynamics

1. Masuda Number

$$\text{Md} = \frac{\rho_l R_0^2 \varepsilon^* E_0^2}{\mu_u^2} \approx 6.374 \times 10^{-2} \quad (\text{D.6})$$

2. Electroinertial Number

$$\mathcal{J}_e = \frac{\rho_l R_0^2}{\varepsilon^* E_0^2 \tau^2} \approx 1.5 \times 10^{-3} \quad (\text{D.7})$$

3. Electroviscous Number

$$\mathcal{V}_e = \frac{\mu_u}{\varepsilon^* E_0^2 \tau} \approx 0.16 \quad (\text{D.8})$$

4. Electrogravity Number

$$\mathcal{G}_e = \frac{gR_0(\rho_l - \rho_u)}{\varepsilon^* E_0^2} \approx 5.5 \times 10^{-3} \quad (\text{D.9})$$

5. Electrocapillary Number

$$\chi_e = \frac{\varepsilon^* E_0^2 R_0}{\gamma} \approx 6.374 \quad (\text{D.10})$$

## E Units associated to electric charge

Unit	Symbol	From “Base Units”	Measures
Coulumb	C	C	Charge
Ampere	A	A = C/s	Current
Volt	V	V = J/C = N m/C	Electric Potential
Ohm	$\Omega$	$\Omega = \text{V/A}$	Resistance
Siemen	S	S = $\Omega^{-1} = \text{A/V}$	Admittance
Farad	F	F = C/V	Capacitance

## DISTRIBUTION:

1	MS 9957	Lindsay Crowl Erickson, 8365
1	MS 9957	Greg Wagner, 8365
1	MS 9957	Jeremy Templeton, 8365
1	MS 9957	Myra Blaylock, 8365
1	MS 9957	Radoslav Bozinoski, 8365
1	MS 9957	Adrian Kopacz, 8365
1	MS 9042	Amanda Dodd, 8365
1	MS 9042	Sarah Scott, 8365
1	MS 9052	Marco Arienti, 8365
1	MS 9957	Victor Brunini, 8365
1	MS 0836	David Noble, 1513
1	MS 0836	Scott Alan Roberts, 1513
1	MS 0828	Jonathan Clausen, 1513
		,
1	MS 0899	Technical Library, 8944 (electronic copy)
1	MS 0359	D. Chavez, LDRD Office, 1911





